Transcriptional remodeling by OTX2 directs specification and patterning of mammalian definitive endoderm

Ee LS[#1], Medina-Cano D[#2], Uyehara CM[1], Schwarz C[3], Goetzler E[1], Salataj E[1], Polyzos A[1], Madhuranath S[1], Evans T[4], Hadjantonakis AK[2], Apostolou E[1], Vierbuchen T[2] and Stadtfeld M[1*]

[1] Sanford I. Weill Department of Medicine, Sandra and Edward Meyer Cancer Center, Weill Cornell Medicine, New York, NY 10065, USA.

[2] Developmental Biology Program, Sloan Kettering Institute, Memorial Sloan Kettering Cancer Center, New York, NY 10065, USA.

[3] Emerald Cloud Lab, Austin, TX 78728 USA.

[4] Department of Surgery, Weill Cornell Medicine, New York, NY 10065, USA; Center for Genomic Health, Weill Cornell Medicine, New York, NY 10065, USA.

#denotes equal contribution

* Corresponding and lead author (mas4011@med.cornell.edu)

- *Mouse and human pluripotent cells with multipurpose degron alleles establish versatile platforms to dissect cell type-specific functions of the pleiotropic transcription factor OTX2*
- *OTX2 controls molecular programs required for anterior-posterior patterning of the developing gut*
- *OTX2 establishes and maintains chromatin accessibility at distinct distal gene regulatory elements in definitive endoderm*
- *OTX2 functions as a patterning factor across different germ layers and species*

Summary

The molecular mechanisms that drive essential developmental patterning events in the mammalian embryo remain poorly understood. To generate a conceptual framework for gene regulatory processes during germ layer specification, we analyzed transcription factor (TF) expression kinetics around gastrulation and during *in vitro* differentiation. This approach identified *Otx2* as a candidate regulator of definitive endoderm (DE), the precursor of all gut-derived tissues. Analysis of multipurpose degron alleles in gastruloid and directed differentiation models revealed that loss of OTX2 before or after DE specification alters the expression of core components and targets of specific cellular signaling pathways, perturbs adhesion and migration programs as well as de-represses regulators of other lineages, resulting in impaired foregut specification. Key targets of OTX2 are conserved in human DE. Mechanistically, OTX2 is required to establish chromatin accessibility at candidate enhancers, which regulate genes critical to establishing an anterior cell identity in the developing gut. Our results provide a working model for the progressive establishment of spatiotemporal cell identity by developmental TFs across germ layers and species, which may facilitate the generation of gut cell types for regenerative medicine applications.

Introduction

Pluripotency exit and morphogenetic changes during gastrulation that result in the acquisition of the germ layers ectoderm, mesoderm, and endoderm are central processes for tissue specification in the post-implantation mammalian embryo and set the stage for later organogenesis (Bardot and Hadjantonakis, 2020; Tam and Behringer, 1997). Genetic studies in model organisms have identified numerous modulators of gastrulation, including regulators of signaling pathways that instruct germ layer identity (Morgani and Hadjantonakis, 2020) and cell surface molecules that promote correct morphogenetic cell migration and adhesion (Muncie et al., 2020). In addition, DNA-binding transcription factors (TFs) have been recognized as important regulators of germ layer and organ specification (Cui et al., 2018; Tam and Loebel, 2007) whose dysregulation can drive developmental and congenital disorders.

Recent single-cell profiling experiments have provided high-resolution atlases of transcriptional changes associated with gastrulation and the emergence of specific germ layers in mouse and human embryos (Nowotschin et al., 2019; Pijuan-Sala et al., 2019; Qiu et al., 2022; Tyser et al., 2021; Zeng et al., 2023). Yet, our understanding of how specific TFs coordinate the transcriptional remodeling required for germ layer specification and organ development at the molecular level remains superficial. This lack of knowledge is due to (i) the inaccessibility of the post-implantation mammalian embryo, (ii) the associated difficulty in generating sufficient cellular material for in-depth molecular characterization of TF functions, and (iii) limitations of existing gene knockout (KO) models concerning specificity and spatiotemporal control, suggesting a need for more tractable experimental systems.

Embryonic stem cells (ESCs) are attractive tools for studying developmental processes (Gaertner et al., 2019). Still, standard mouse ESC (mESC) differentiation protocols are highly variable and yield disorganized and/or heterogeneous cell populations that inadequately mirror embryonic patterning processes (Bernardo et al., 2011; Drukker et al., 2012; Yu et al., 2011). Human ESCs (hESCs) achieve more homogenous differentiation responses upon suitable stimulation (Hawkins et al., 2021; Loh et al., 2014; Pan et al., 2020), possibly because they resemble a post-implantation "primed" state of development (Tesar et al., 2007). Accordingly, converting naïve mESCs into a primed state allows near-homogenous, signaling-mediated differentiation into tissues such as definitive endoderm (DE), the precursor of all gut-derived organs (Medina-Cano et al., 2022). For the interrogation of protein function, in-frame fusions of

3

94 degron tags such as FKBP12^{F36V} (referred to as the dTAG system) (Nabet et al., 2018) to

95 proteins of interest has emerged as a powerful approach to enable acute, controlled and specific

96 depletion of candidate factors (Jaeger and Winter, 2021; Prozzillo et al., 2020), which has been

97 applied to address developmental questions (Abuhashem et al., 2022; Bisia et al., 2023).

98 Integrating degron alleles into synchronized directed differentiation regimens, therefore, in

99 principle, represents a tractable and versatile experimental platform to dissect the function of

100 developmental TFs at high temporal resolution.

101 OTX2 is a conserved homeobox TF with pleiotropic functions during vertebrate

102 development (Beby and Lamonerie, 2013). In mouse and other animal models, OTX2 is required

103 for correct migration and inductive properties of the anterior visceral endoderm (Rhinn et al.,

104 1998), an extra-embryonic tissue required for establishing anterior-posterior identity in the

105 mammalian embryo. Subsequently, OTX2 by cell-autonomous and non-autonomous

106 mechanisms (Rhinn et al., 1999) controls the specification and patterning of the neuroectoderm

107 (Acampora et al., 1995) and later the formation of specific neuroectoderm derivatives (Beby and

108 Lamonerie, 2013). Gastrulation-stage mouse embryos deficient for OTX2 manifest with defects

109 in non-ectodermal tissues, including foregut and heart abnormalities (Ang et al., 1996; Jin et al.,

110 2001; Matsuo et al., 1995) suggesting OTX2 functions in germ layers beyond ectoderm.

111 By mining published and unpublished genomics datasets, we identified evidence for a

112 direct role of OTX2 in the formation and patterning of the mammalian DE and primary gut tube.

113 Systematic assessment of embryonic endoderm formation from mouse and human primed

114 pluripotent stem cells harboring "multipurpose" (degradation/immunoprecipitation/visualization)

115 degron alleles showed that stage-specific depletion of OTX2 resulted in abnormal DE with

116 impaired ability for anteriorization and foregut differentiation. Transcriptional functions of OTX2

117 in the DE include the activation of specific gut tube-associated downstream TFs, balanced

118 expression of WNT and FGF/ERK signaling components, and repression of non-endodermal

119 genes. Gene activation by OTX2 entails OTX2-dependent gain of chromatin accessibility at

120 distal enhancer elements harboring canonical binding motifs, some of which are primed for

121 activation by OTX2 binding in the epiblast. In contrast, OTX2-dependent gene repression

122 proceeds via binding to low-affinity sites and by indirect mechanisms. Our results suggest that

123 OTX2 is a central component of a transcriptional program for anteriorization during peri-

124 gastrulation phases of development that is conserved across germ layers and species.

4

Results

Integrative analysis of in vivo and in vitro datasets identifies candidate regulators of germ layer specification

We analyzed available genomics and phenotypic data to identify candidate transcriptional regulators of germ layer specification among a comprehensive list of 1,682 murine TFs (Garipler et al., 2022). We set as criteria **I)** strong upregulation – fold change (FC)>5 and adjusted p-value (padj) <0.05 – during the transition of mESCs to epiblast-like stem cells (EpiLCs) which resemble the early post-implantation epiblast (Hayashi et al., 2011) (**Table S1**), consistent with a role in preparing for germ layer specification; **II)** sustained elevated expression throughout formation and patterning of at least one germ layer in the mouse embryo based on single-cell RNA sequencing (scRNA-seq) (Nowotschin et al., 2019; Pijuan-Sala et al., 2019) and **III)** developmental organ phenotypes in KO mice in the Mouse Genome Database (Bult et al., 2019). This approach resulted in the identification of a group of seven candidate TFs that met all criteria (**Fig.S1A**). Among these candidates, *Otx2* – encoding an essential and highly conserved homeobox TF (Ang et al., 1996; Matsuo et al., 1995) – demonstrated the most significant upregulation during the transition from naïve to primed pluripotency (**Table S1**). While the importance of OTX2 for development of the anterior visceral endoderm and anteriorization of the neuroectoderm (NE) have been documented (Acampora et al., 1995; Hever et al., 2006; Simeone, 1998), we also observed *Otx2* expression along the trajectory of early gut tube development in the mouse embryo (post-implantation epiblast → anterior primitive streak → definitive endoderm (DE) → anterior gut tube) (**Fig.1A,B**). *Otx2* levels in DE were comparable to those in VE and NE (**Fig. S1B**), consistent with an unexplored role of this TF in the embryonic endoderm.

To enable studies into developmental functions of OTX2, we used Cas9-faciliated gene targeting to generate several mESC lines homozygous for a "multipurpose" degron allele. In addition to a dTAG fusion (Nabet et al., 2018) for controlled protein degradation, this allele contains an HA tag fusion to enable immunoprecipitation (IP) and immunofluorescence (IF) independent of the availability of TF-specific antibodies, and a transcriptional reporter encoding a nuclear-localized EGFP (**Fig.1C**). Flow cytometric analysis revealed a low level of *Otx2* expression in mESCs, but significant upregulation in derivative EpiLCs and epiblast stem cells (EpiSCs) (**Fig.S1C**), representing two successive stages of the post-implantation epiblast before

5

156 germ layer specification. This observation is consistent with previous results (Buecker et al.,

157 2014) and *Otx2* expression kinetics *in vivo* (Acampora et al., 2013). Treatment of OTX2-dTAG

158 EpiLCs with the inducer molecule dTAG-13 resulted in reproducible and highly efficient (>90%)

159 degradation of OTX2 within one hour (h) of culture (**Fig.1D**), documenting our ability to acutely

160 control OTX2 levels.

161

OTX2 depletion impairs DE formation from mouse pluripotent stem cells

163 To explore the role of OTX2 during differentiation, we converted EpiLCs derived from OTX2-

164 dTAG mESCs into anterior primitive streak derivatives that emerge during gastrulation using

165 micropattern technology (Morgani et al., 2018)(**Fig.S1D**). Immunostaining revealed a

166 quantitative reduction in the number of cells expressing the DE marker SOX17 (Kanai-Azuma et

167 al., 2002; Morgani et al., 2018) after depletion of OTX2 at the onset of differentiation. In contrast,

168 FOXA2$^+$SOX17$^-$ putative axial mesoderm cells were still efficiently formed (**Fig.1E,F**). We also

169 observed a slight increase in the levels of the epiblast marker SOX2 with loss of OTX2

170 (**Fig.1E,F**). These observations demonstrate perturbed gastruloid formation without OTX2 and

171 suggest a previously unappreciated and specific role of this TF for DE development.

172 To further dissect the molecular function of OTX2 during DE development, we

173 implemented a recently published directed differentiation approach which efficiently converts

174 EpiSCs into primitive streak (PS) (via transient WNT activation) followed by DE (via BMP

175 inhibition and high levels of Activin A/Nodal signaling) (Medina-Cano et al., 2022) (**Fig.1G**). We

176 established and validated stable homozygous OTX2-dTAG EpiSC lines and differentiated them

177 towards DE, confirming expression of canonical protein markers OCT4 (EpiSC/PS), T(PS) and

178 SOX17 (DE) by the majority (>90%) of cells at the expected timepoints (**Fig.S1E**). *Otx2*

179 expression (measured by *Otx2*-EGFP or HA IF) was detected in >95% of cells at all stages and

180 gradually increased in intensity with highest levels attained in DE (**Fig.1H**), but OTX2 levels were

181 reduced to background after 1h of culture of PS or DE in presence of dTAG-13 (**Fig.S1F**). OTX2

182 depletion at the PS stage (i.e., concurrent with DE specification) (**Fig.1G**) resulted in reduced

183 differentiation into DE (CXCR4$^+$PDGFRA$^-$ cells), with a concordant increase in PDGFRA$^+$

184 putative early mesodermal cells (Takenaga et al., 2007) (**Fig.S1G** and **Fig.1I**). In addition, we

185 observed reduced levels of the DE-associated TF SOX17 (**Fig.1J**). This effect was specific to

186 OTX2-dTAG cell lines treated with degrader, as dTAG-13 treatment did not affect SOX17

6

187   expression in parental (WT) cells (**Fig.S1H**) and DE differentiation was unaffected by DMSO

188   treatment (vehicle control) in OTX2-dTAG cells (**Fig.S1G**).

189   These findings suggest that OTX2 is important for differentiation towards DE and,

190   possibly, away from mesoderm. OTX2 works in a partially cell non-autonomous manner during

191   anterior neuroectoderm induction (Rhinn et al., 1999). However, analysis of DE established after

192   mixing different ratios of OTX2-dTAG and parental (WT) EpiSCs, revealed no evidence for

193   rescue of CXCR4 levels in OTX2-depleted cells by WT cells or reduced CXCR4 levels in WT

194   cells in presence of OTX2-depleted cells (**Fig.S1I**). These observations support the cell-

195   autonomous functions of OTX2 in driving DE-associated gene expression.

196

197   ***OTX2 loss affects specific developmental programs during DE specification and***

198   ***maintenance***

199   To characterize transcriptional consequences of OTX2 depletion during DE specification on a

200   genome-wide scale and at single cell resolution, we applied single cell RNA sequencing (scRNA-

201   seq) analysis (10X Genomics platform). For this, we used cells generated with the directed

202   differentiation paradigm described above. Multiplexed samples – EpiSCs, DE derived in

203   presence of DMSO (control DE) and DE after OTX2 depletion in PS when induced to become

204   DE (OTX2$^{depl\_PS}$ DE) – were subjected to standard processing and QC procedures including

205   elimination of background reads and low-quality cells (Fleming et al., 2022) and analyzed with

206   Scanpy (Wolf et al., 2018). Both control and OTX2 depleted DE clustered away from EpiSCs

207   and showed extinction of pluripotency-associated transcripts, absence of markers for visceral

208   (*Sox7*) and primitive (*Ttr*) endoderm, as well as high levels of a subset of DE-specific markers

209   such as *CD24a*, *Larp7* and *Hhex* (Moore et al., 2014; Pijuan-Sala et al., 2019; Wang et al., 2012)

210   (**Fig.S2A**). We also did not observe differences in cell cycle state based on expression of the

211   G2/M indicators *Aurka* and *Plk1* (Liu et al., 2022) (**Fig.S2A**).

212   Nevertheless, OTX2$^{depl\_PS}$ DE formed a distinct cluster on the UMAP projection (**Fig.2A**

213   and **Fig.S2B**), suggesting that OTX2 depletion redirects the developmental trajectory of DE

214   formation from the epiblast and results in a distinct transcriptional state. Accordingly, we

215   identified a total of 1,646 differentially expressed genes (DEGs) (RNA

216   score>1;logFC>1;padj<0.05) between control and OTX2$^{depl\_PS}$ DE (**Table S2**), similar fractions

217   of which were downregulated (44.9%) or upregulated (55.1%) (**Fig.2B**). Gene ontology analysis

7

218 of DEGs suggested dysregulation of WNT signaling, cell adhesion/migration and cell

219 differentiation in absence of OTX2 (**Fig.2C**). At the gene level, we observed downregulation of

220 DE-associated TFs (such as *Sox17* and *Hesx1*), antagonists of WNT signaling (*Dkk1*, *Shisa2*)

221 and cell migration/adhesion regulators (*Cdh1*, *Sema6d* and *Emb*) in OTX2$^{depl\_PS}$ DE (**Fig.2D** and

222 **Fig.S2C**). Upregulated genes included agonist and canonical targets of WNT and

223 FGF/regulators (*Cdh2, Sema3a*) (**Fig.2D** and **Fig.S2C**).

224 Of note, we also observed significant upregulation of several TFs (*Prdm6*, *Mixl1* and

225 *Tfap2c*) (**Fig.2D** and **Fig.S2C**) associated with other embryonic lineages emerging in early post-

226 gastrulation embryos, including mesoderm, neuroectoderm and primordial germ cells (PGCs)

227 (**Fig.S2D**). We also confirmed upregulation of mesoderm associated *Pdgfra* (**Fig.S2E**).

228 Importantly, ectopic lineage markers were co-expressed in OTX2$^{depl\_PS}$ DE at the single cell level

229 (**Fig.S2E**), suggesting that OTX2 loss does not result in the emergence of multiple distinct

230 lineages but rather to partial derepression of specific non-endodermal markers in the same cells.

231 Together, these observations demonstrate that loss of OTX2 during DE specification results in

232 the dysregulation of specific gene expression programs and a profound redirection of DE

233 identity. We confirmed dysregulation of major genes representing the affected programs (TFs,

234 WNT and FGF/signaling and cell adhesion/migration) upon OTX2 depletion at PS in an

235 independent cell line (**Fig.S2F**).

236 To compare molecular consequences when losing OTX2 before or after endodermal

237 identity has been established (Medina-Cano et al., 2022), we depleted OTX2 24h after initiation

238 of DE specification, followed by scRNA-seq analysis. This strategy resulted in a similar number

239 of DEGs (n=1,477) than depletion at PS (**Fig.S2G)** with overall concordant gene expression

240 changes triggered by OTX2 loss before and after DE specification (**Fig.2E**). For example,

241 hallmark molecular changes observed upon OTX2 loss at PS – such as dysregulated expression

242 of WNT/FGF signaling components and of cell adhesion/migration regulators as well as reduced

243 levels of DE markers – were also observed in OTX2$^{depl\_DE}$ DE (**Fig.2E**). However, elevated

244 expression of genes associated with nascent mesodermal lineages such as *Eomes*, *T*, *Prdm6*

245 and *Pdgfra* was more pronounced in OTX2$^{depl\_PS}$ DE (**Fig.2E**), suggesting that a repressive role

246 of OTX2 at these loci may no longer be required once DE has been specified.

247 Many of the shared gene expression changes induced by OTX2 depletion before or after

248 DE specification – such as the observed evidence for increased WNT and FGF/ERK signaling

249   (Loh et al., 2014; Pan et al., 2020) – are consistent with loss of anterior-posterior (AP) identity.

250   Indeed, evaluation of the relative expression levels of a panel of marker genes for different

251   endodermal lineages along the AP axis (Pijuan-Sala et al., 2019) revealed a pronounced deficit

252   in the expression of specific anterior markers in the absence of OTX2 (**Fig.2F**). Accordingly,

253   further differentiation of OTX2-depleted DE towards the foregut lineage (**Fig.2G**) revealed an

254   impairment to form clusters of SOX2$^+$PDX1$^+$ gastric progenitors (Medina-Cano et al., 2022).

255   Evidence for altered foregut development were observed independently of whether OTX2 was

256   depleted at the PS stage or after DE specification (**Fig.2H** and **Fig.S2H**). These molecular and

257   functional analyses document that OTX2 contributes to establishing and maintaining gene

258   expression programs required for successful anteriorization of the developing DE.

259

260   ***OTX2 drives locus-specific chromatin remodeling during DE specification***

261   Having established a requirement of OTX2 for proper specification and anterior patterning of

262   DE, we next sought to investigate the mechanisms of gene regulation by OTX2 during DE

263   specification. To identify potentially direct OTX2 targets in EpiSCs and DE, we conducted

264   CUT&RUN experiments with a validated antibody (Alexander et al., 2018; Seah et al., 2019)

265   against the HA epitope that is part of our multipurpose degron allele (**Fig.1C**). CUT&RUN

266   revealed 1,286 high-confidence OTX2 binding sites (see Methods section) that were unique to

267   undifferentiated EpiSCs ("EPI peaks"), 5,035 binding sites shared between EpiSCs and DE

268   (referred to as "primed DE peaks" hereafter) and 37,676 OTX2 bindings unique to DE 24h after

269   induction from PS (referred to "*de novo* DE peaks") (**Fig.3A**). In contrast, HA CUT&RUN in

270   wildtype DE (i.e., not carrying the HA epitope) revealed only background signal (**Fig.S3A**),

271   supporting the specificity of OTX2 detection. The drastic increase in the number of OTX2 binding

272   sites – and the elevated strength of primed peaks from EpiSCs to DE (**Fig.S3B**) – coincides with

273   the marked transcriptional upregulation of *Otx2* during DE specification (see **Fig.1H**) and

274   indicates extensive reorganization of the OTX2 cistrome during this developmental transition.

275   EPI and *de novo* DE peaks both were most frequent at intronic and distal intergenic sites

276   (**Fig.S3C**) and enriched for genes associated with stage-specific developmental functions, such

277   as Activin receptor signaling and multilineage differentiation (EPI peaks) or cell migration and

278   primitive streak formation (DE peaks) (**Fig.3B**). For example, EpiSC-specific binding was evident

279   at *Pou5f1*, a pluripotency associated locus previously reported to be regulated by OTX2 (Di

280   Giovannantonio et al., 2021) (**Fig.S3D**), and occurred at sites enriched for binding motifs of

281   pluripotency-associated TFs (OCT4, SOX2, OCT6) (**Fig.3C**). In contrast, *de novo* peaks were

282   enriched for binding motifs of TFs with known functions in endoderm development (such as

283   GSC, FOXA1, GATA4) (**Fig.3C**). Primed DE peaks were frequently promoter proximal (**Fig.S3C**)

284   and enriched for genes associated with universal cellular processes such as protein quality

285   control and Rac signaling (**Fig.3B**) as well as for motifs of non-cell type specific TFs (**Fig.3C**),

286   possibly reflecting their position within promoters. These observations document that OTX2

287   occupies candidate regulatory elements of critical lineage-associated genes in a stage-specific

288   manner, likely in collaboration with other developmental TFs.

289   We observed well-defined OTX2 peaks at many DEG^{DOWN} and DEG^{UP}, representing the

290   major cellular programs transcriptionally dysregulated upon OTX2 depletion (**Figs.3D,E** and

291   **Table S3**). To systematically investigate the relationship between OTX2 binding and the

292   transcriptional responses triggered by its loss, we analyzed frequency, strength, genomic

293   positioning, and developmental dynamics of OTX2 peaks at genes affected by OTX2 depletion.

294   To reduce the impact of lowly expressed genes on this analysis, we focused on DEGs with an

295   RNA score>10, covering 448 DEG^{UP} and 393 DEG^{DOWN} (**Table S2**). As reference, we used 1,169

296   gene loci expressed in DE but unaffected (padj>0.9) by OTX2 depletion. In accordance with a

297   direct role of OTX2 in controlling DE transcription) we observed that >80% of DEG^{DOWN} and

298   >75% of DEG^{UP} but only slightly less than 50% of unaffected loci were bound at least once by

299   OTX2 at their promoters or distal regions(**Fig.S3E**). OTX2-bound DEGs on average also showed

300   a significantly higher number of OTX2 peaks than unaffected genes (**Fig.S3F**). In a clear

301   distinction, OTX2 peaks at DEG^{DOWN} were significantly stronger than peaks at DEG^{UP} and at

302   unaffected genes (**Fig.S3G** and **Fig.3D,E**). We also observed a pronounced enrichment of

303   DEG^{DOWN} but not of DEG^{UP} in vicinity of the strongest peaks (4th quartile; Q4) (**Fig.3F**). This

304   suggests that the locus-specific regulatory function of OTX2 (activator versus repressor) may in

305   part be determined by the affinity of its target cis regulatory elements, as has been proposed for

306   homeobox TFs in other developmental contexts (White et al., 2016).

307   Despite the overall low abundance of primed peaks (11.8%) among all DE-associated

308   peaks (**Fig.3A**), more than a quarter (26.3%) of DEG^{DOWN} showed evidence for OTX2 binding in

309   EpiSCs (**Fig.3G**) with almost all DE-associated loci that were already bound by OTX2 in EpiSCs

310   acquiring additional peaks upon differentiation (**Fig.S3H** and **Fig.3D,E**). Consistent with a

10

311   priming function of OTX2 before DE differentiation, genes with primed peaks were already

312   expressed at higher levels in EpiSCs before becoming further upregulated during DE

313   specification (**Fig.3H**). Both primed and *de novo* bound loci enriched for genes encoding

314   regulators of cell adhesion and migration (such as *Emb*, *Robo1* and *Sema6d*) and antagonists

315   of WNT signaling (*Dkk1* and *Shisa2*) (**Fig.3G**). In contrast, DEG^{DOWN} loci encoding TFs

316   regulating DE and derivative anterior lineages such as *Hesx1*, *Sox17* and *Isl1* were bound by

317   OTX2 in DE only (**Fig.3D,G** and **Table S3**). These observations are consistent with the notion

318   that OTX2 binding in the epiblast primes transcriptional programs broadly required for

319   gastrulation and germ layer formation. The full activation of OTX2-controlled DE-specific genes,

320   however, requires additional regulatory remodeling upon receipt of developmental signals.

321

322   ***OTX2 functions partially by controlling chromatin accessibility at development loci***

323   We next examined to what degree stage specific OTX2 binding impacts chromatin accessibility

324   during DE differentiation. When focusing on differentially accessible regions (DARs) between

325   EpiSCs and DE (Medina-Cano et al., 2022), we noticed that more than 40% of DE-specific DARs

326   (n=20,475) overlapped with OTX2 target sites (either primed or *de novo*) (**Fig.S4A**), while the

327   vast majority (~90%) of EpiSC DARs did not. To test experimentally whether OTX2 binding

328   actively contributes to chromatin opening during endoderm specification, we performed ATAC-

329   seq analysis of DE 24h after OTX2 depletion at the PS stage. This revealed 3,381 high-

330   confidence DARs (logFC>1;padj<0.05) compared to DMSO-treated controls. Among DARs,

331   26.1% showed elevated and 73.9% reduced ATAC-seq signal (**Fig.4A** and **Fig.S4B**),

332   demonstrating that OTX2 favors the establishment or maintenance of accessible chromatin in

333   DE. The majority but not all chromatin changes induced by OTX2 depletion occurred at sites

334   normally undergoing accessibility changes during DE specification (**Fig.S4C**).

335   Supervised clustering of all lost or gained DARs upon dTAG-13 treatment in DE along

336   with their accessibility levels in wildtype EpiSC, generated four distinct ATAC-seq peak clusters

337   (C1-C4). C1 genomic sites (n=1,091) were accessible in EpiSCs and DE but lost accessibility in

338   DE upon OTX2 depletion, whereas C2 sites (n=1,508) normally gained accessibility in DE but

339   failed to do so in absence of OTX2 (**Fig.4B**). Both C1 and C2 DARs were enriched at promoter

340   distal regions (**Fig.S4D**) and showed strong, OTX2-dependent transcriptional upregulation of

341   associated genes during DE specification (**Fig.4C**). In total, 32.6% of DEG^{DOWN} were associated

11

342 with local loss of chromatin accessibility upon OTX2 depletion (**Fig.S4E**), including gene loci

343 encoding negative regulators of WNT signaling (*Dkk1, Sfrp5*), cell type-specific transcription

344 (*Hesx1, Isl1*) and cellular migration/adhesion (*Emb, Sema6d*) (**Fig.4D** and **Table S4**).

345 Importantly, most C1 and C2 DARs were bound by OTX2 (**Fig.4E**) with strongest binding at C1

346 (**Fig.S4F**). These observations support a direct role of OTX2 in controlling chromatin

347 accessibility and transcriptional output at these loci. The regulatory function of OTX2 at a subset

348 of C1 sites includes preoccupancy in EpiSCs (**Fig.4E**). Of note, while binding motifs of OTX2

349 and SOX factors were enriched at both C1 and C2 DARs (**Fig.4F and S4G**), TCF4, NR6A1 and

350 pluripotency factors NANOG and OCT4 were predominantly associated with C1 DARs only and

351 GATA factors with C2 DARs only (**Fig.4F and S4G**). These observations suggest that OTX2-

352 dependent chromatin opening during DE specification enables binding of additional, stage-

353 specific co-regulators.

354   As mentioned above, OTX2 depletion also resulted in gain of chromatin accessibility (C3

355 and C4 DARs). C3 sites (n=489) were pre-accessible in EpiSCs and failed to appropriately close

356 in DE upon OTX2 depletion, whereas C4 sites (n=393) were normally closed in both EpiSCs and

357 DE but aberrantly gained accessibility in DE in absence of OTX2 (**Fig.4B**). Concordantly, genes

358 associated with C3 and C4 peaks showed transcriptional upregulation upon OTX2 depletion

359 (**Fig.4C**). Strikingly, the majority of C3 and C4 DARs did not overlap with OTX2 binding sites

360 (**Fig.4E**), suggesting indirect activation of most of these loci downstream of OTX2 loss.

361 Moreover, even C3/C4 DARs bound by OTX2 were not enriched for the OTX2 consensus motifs

362 (**Fig.S4G**), supporting the notion that binding of OTX2 to loci it represses is mechanistically

363 distinct from OTX2 binding to loci this TF activates. C3/C4 DARs were enriched for a distinct set

364 of regulators than C1/C2 DARs, including the endomesodermal TFs EOMES and FOXA2 and

365 the WNT mediators TCF7L1/2 (**Fig.4F and S4G**). This observation suggests that OTX2 loss

366 increases levels and/or activity of these factors, resulting in ectopic chromatin activation.

367 Together, these observations show that OTX2 engages in both activating and repressive

368 functions during DE specification and exerts part of its activator function by maintaining pre-

369 existing and establishing new chromatin accessibility at distal gene regulatory elements that

370 control the expression of endoderm-associated genes.

371

372 ***OTX2 is required for faithful specification of human DE***

12

Compared to most other TFs associated with endodermal differentiation, OTX2 has an unusual high degree (99.7%) of amino acid sequence conservation between mouse and human (Cunningham et al., 2022) (**Fig.S5A**). This suggests evolutionary pressure to preserve protein function and establishes a unique opportunity to study shared and species-specific cis-regulatory aspects of transcriptional control during endoderm specification. To determine the role of OTX2 during human DE development, we established homozygous human embryonic stem cell (hESC) lines carrying the identical multipurpose degron cassette we employed in mouse (**Fig.5A**). For this, we used MEL-1 and H9 hESCs, two well-characterized lines with established DE potential (Chia et al., 2019; Jiang et al., 2013). In both parental backgrounds, the hOTX2-dTAG allele allowed rapid (1h) and efficient (>90%) OTX2 depletion in hESC and derivative DE (**Fig.5B**), using the degrader dTAG-v1 (Nabet et al., 2020) which we found more effective in human cells than dTAG-13 (**Fig.S5B**).

We differentiated OTX2-dTAG hESCs towards DE with two slightly different protocols – one using identical signaling manipulations to the one applied in mouse ("Protocol 1") (Medina-Cano et al., 2022), the other applying additional PI3K inhibition during PS specification ("Protocol 2") (Loh et al., 2014) (**Fig.S5C**). In accordance with the developmental resemblance of human pluripotent cells to the post-implantation epiblast, we observed widespread *OTX2* expression in OTX2-dTAG hESCs (**Fig.S5D**), mirroring the situation in mouse EpiSCs and EpiLCs (**Fig.S1C**). *OTX2* expression levels strongly increased during commitment to human DE (**Fig.S5E**), as we also had observed in mouse (**Fig.1H**), suggesting similarities in the manner the *OTX2* locus is controlled by external signaling cues in both species.

Differentiation of OTX2-dTAG hESCs towards endoderm in the absence of dTAG-v1 yielded predominantly cells co-expressing the DE markers CXCR4 and CD117 (**Fig.5C,D**), demonstrating that the degron allele does not interfere with endodermal differentiation. In contrast, depletion of OTX2 from the PS stage onwards resulted in significantly fewer CXCR4$^+$CD117$^+$ cells (**Fig.5C,D**). Analysis by qPCR of select gene loci representing pathways and processes that are affected by OTX2 depletion in mouse DE, revealed evidence for dysregulation of similar developmental modules. Thus, we observed altered expression of developmental TFs, including lower levels of the DE-associated TF *HESX1* and elevated levels of "ectopic" TFs such as *MIXL1* and *TFAP2C* in human DE specified in the absence of OTX2 (**Fig.5E**). In contrast, SOX17 levels were not downregulated at RNA or protein level in human

13

404 DE upon OTX2 depletion (**Fig.5E** and **Fig.S5F**), suggesting differences in the regulation of this

405 locus between mouse and human DE (see **Fig.1J** and **Fig.2D**).

406 Expression changes of genes encoding WNT and FGF/ERK signaling components

407 changed in a manner consistent with activation of these two pathways in human DE in the

408 absence of OTX2 (**Fig.5E**), similar to what we had observed in mouse DE. While levels of the

409 transcriptional OTX2-EGFP reporter were only moderately affected by OTX2 depletion (**Fig.5F**),

410 fluorescence microscopy showed that EGFP$^+$ human DE lacking OTX2 protein failed to form the

411 dense cell clusters that were abundant in endodermal cultures expressing this TF (**Fig.5G**). This

412 suggests a deficit in the ability of OTX2-deficient DE to self-organize that is reminiscent of the

413 observations made in mouse foregut (see **Fig.2H and S2H**). Together, these observations are

414 consistent with the notion that OTX2 is an important regulator of human gut tube specification

415 and suggest that specific developmental functions of this TF are conserved between mice and

416 humans (**Fig.5H**).

417

418 **Discussion**

419 To facilitate studying TF function during mammalian germ layer specification, we implemented

420 an experimental platform that combines efficient and scalable *in vitro* models of embryonic

421 lineage specification with genetic tools for controlled protein degradation. Taking this

422 generalizable approach, we have identified and characterized a previously unappreciated role

423 of OTX2 in DE specification and patterning. In contrast to other TFs regulating endoderm

424 development such as SOX17 (Kanai-Azuma et al., 2002) or the early endomesodermal

425 specification factor EOMES (Arnold et al., 2008) whose loss in KO mouse models results in

426 entire parts of the early gut tube missing, OTX2 depletion in our system does not result in a

427 complete loss of endoderm identity or the generation of non-viable cells. Rather, acute

428 degradation of OTX2 during or after DE formation leads to incorrect patterning with OTX2-

429 depleted DE characterized by dysregulation of WNT and FGF/ERK signaling, altered expression

430 of migratory and cell adhesion molecules, as well as ectopic expression of regulators of other

431 early embryonic lineages. These abnormalities prevent the faithful establishment of anterior

432 endoderm identity. Our results are in accordance with the mislocalization of endomesodermal

433 cells and impaired foregut formation in OTX2 KO mice (Acampora et al., 1995; Kimura et al.,

434 2000).

14

435   At the molecular level, OTX2 binds to distal gene regulatory elements at loci encoding

436   regulators of cellular signaling, cell adhesion, and gut tube development such as *Dkk1*, *Cdh1*,

437   *Hesx1*, and *Isl1*. At these loci, OTX2 is required to establish and maintain chromatin accessibility.

438   These observations establish OTX2 as a direct regulator of – and potential pioneer factor for –

439   a subset of candidate enhancers involved in DE specification and patterning. Of note, at several

440   genes encoding known regulators of gastrulation and/or gut tube development, OTX2 binding

441   precedes transcriptional upregulation. This suggests a priming function of OTX2 binding in the

442   epiblast, reminiscent of the pre-positioning reported for other TFs, such as OCT2, during

443   lymphocyte development (Doane et al., 2021). The changes in OTX2 genome binding we

444   observed between epiblast and endoderm continue the genome occupancy dynamics initiated

445   when this TF becomes activated upon exit from naïve pluripotency (Navarra et al., 2016; Yang

446   et al., 2014). While requiring further investigation, it is plausible that *de novo* OTX2 binding in

447   DE is driven partly by the availability of different co-factors (resulting in a shift away from sites

448   occupied by pluripotency-associated factors such as OCT4 and towards sites occupied by

449   endoderm regulators such as SOX2/SOX17 and GATA factors) and partly by the elevated OTX2

450   levels in DE (possibly resulting in occupation of low-affinity binding sites). The observation that

451   only comparatively few OTX2-bound genes are differentially expressed upon OTX2 loss might

452   suggest promiscuous binding or redundancy with another TF. On the other hand, not all OTX2-

453   regulated genes (i.e., bound by OTX2 and downregulated in dTAG conditions) lose chromatin

454   accessibility upon OTX2 depletion. This points to additional mechanisms beyond chromatin

455   opening that OTX2 may employ to drive gene expression, such as changes in enhancer activity

456   and/or chromatin looping (Uyehara and Apostolou, 2023).

457   We observed aberrant chromatin opening upon OTX2 depletion at only a subset of gene

458   loci upregulated in the absence of OTX2, suggesting that gene repression by this TF is primarily

459   mediated by a mechanism not affecting chromatin accessibility. Of note, studies in frogs have

460   suggested that OTX2 can directly exert both activating and repressive functions, depending on

461   the nature of cis-regulatory elements it binds to and the co-factors it engages with (Yasuoka et

462   al., 2014). In agreement with this, we observed weaker binding of OTX2 to gene loci it represses

463   and no enrichment of the OTX2 consensus motif at sites gaining chromatin accessibility in the

464   absence of this TF. We surmise that OTX2 achieves gene repression in DE by a variety of direct

15

465 and indirect mechanisms, including counteracting the expression and/or activity of TFs driving

466 alternative lineages and suppression of WNT signaling.

467 Our stage-specific deletion experiments demonstrate a requirement for OTX2 beyond DE

468 specification. In fact, most genes and developmental programs affected in DE upon OTX2 loss

469 before or after endoderm specification are shared. Intriguingly, high levels of *Otx2* expression

470 are maintained at least until the anterior foregut and possibly beyond in thyroid and thymus

471 progenitors (Nowotschin et al., 2019), raising the possibility that OTX2 functions throughout the

472 progressive anteriorization of the developing gut tube. The similar expression kinetics of

473 *Otx2/OTX2* during the early stages of mouse and human *in vitro* development, the enrichment

474 of the OTX2 motif at mesendodermal enhancers during hESC differentiation (Tang et al., 2022)

475 , and our limited analysis of gene expression changes at murine OTX2 target genes in OTX2-

476 depleted human DE, suggests at least partial conservation of OTX2 function during mammalian

477 evolution. Furthermore, the observation that some of the OTX2 targets we identified in DE are

478 shared with other lineages, including *Dkk1* in the anterior visceral endoderm (Kimura-Yoshida

479 et al., 2005) and *Hesx1* in the forebrain (Spieler et al., 2004), supports the existence of a shared

480 molecular blueprint of AP patterning that employs OTX2. The full repertoire of stage-specific

481 versus tissue-specific versus species-specific versus "universal" OTX2 target genes – and the

482 mechanisms of their regulation by OTX2 – remains to be determined.

483 Upon OTX2 depletion, we observed elevated expression of some signaling and

484 transcriptional regulators associated with the primitive streak and/or the early mesoderm

485 (*Pdgfra, Fgf8, Mixl1, Eomes, Prdm6*), the germline (*Tfap2c)* and, to a more limited degree, the

486 neuroectoderm (*Zic2, Zic5*). The de-repression of *Tfap2c/TFAP2C*, which encodes a TF required

487 for germline development (Kojima et al., 2021), is consistent with a germline-repressive function

488 of OTX2 in mice (Zhang et al., 2018) and humans (Tang et al., 2022). Based on these

489 observations, we speculate that OTX2 facilitates the timely establishment of an endodermal

490 identity in the anterior primitive streak by selectively targeting master regulators of alternative

491 embryonic cell types rather than broadly suppressing the gene expression programs of these

492 lineages. Of note, in an *in vitro* system of mouse PGC formation, OTX2 depletion favors

493 germline over mesoderm differentiation (Di Giovannantonio et al., 2021). This suggests stage-

494 specific functions of OTX2 in somatic lineage specification beyond neuroectoderm and DE, a

495 notion consistent with the expression pattern of *Otx2* in gastrulation-stage embryos (**Fig.1B**).

16

496   An ability of OTX2 to directly counteract posterior development has been suggested by
497 microinjection experiments in the frog (Pannese et al., 1995). While further experiments are
498 required to address such an OTX2 function during mammalian development, our scRNA-seq
499 analysis at the DE stage shows no evidence for the upregulation of hindgut regulators or
500 signature genes. This might suggest that OTX2 primarily acts to activate anterior DE loci or
501 reflects the fact that culture conditions employed here are not permissive for posterior gut tube
502 differentiation. The general notion of OTX2 being a gastrulation and germ layer regulator rather
503 than a pluripotency regulator is consistent with the survival of OTX2 KO mice until early
504 organogenesis (Ang et al., 1996) and the mild and delayed defects in mouse pluripotent stem
505 cell lines upon OTX2 deletion (Acampora et al., 2013; Kinoshita et al., 2020).

506   In summary, our studies provide insight into the transcriptional regulation of early gut tube
507 patterning by OTX2 and suggest similarities in the molecular control of anteriorization across
508 tissues and species. The integration of multipurpose degron alleles into efficient directed
509 differentiation regimens of pluripotent cells represents a tractable and readily generalizable
510 platform to dissect these similarities further and to study other developmental processes in
511 mammals.

512

523

Author contributions

524 **Author contributions**
525 L.E. generated and characterized murine cell lines, conducted, and analyzed directed
526 differentiation experiments, prepared cells for genomics assays and assisted in micropattern

527   differentiation. D.M. conducted bioinformatics analyses and assisted with foregut differentiation

528   experiments. C.U. conducted CUT&RUN experiments and assisted in bioinformatics analyses.

529   C.S. conducted micropattern experiments. E.S. conducted ATAC-seq experiments. A.P.

530   assisted with bioinformatic analyses. S.M. assisted in characterizing mouse and human degron

531   cell lines. M.S. and E.G. generated human, validated, and differentiated human degron cell lines.

532   The manuscript was written by M.S. and edited by L.S., C.U., D.M., with input from all authors.

533   M.S. acquired funding. T.E., A.K.H., E.A. and T.V. advised on experimental design, provided

534   reagents, and supervised experiments.

535

536   **Declaration of interests**

537   The authors declare no competing interests

538

539   **Figure titles and legends**

540

541   **Figure 1. OTX2 depletion impairs DE development in murine models of germ layer**

542   **specification**

543   A. *Otx2* expression levels in gastrulation-stage (E6.5-8.5) mouse embryos (modified after

544   Pijuan-Sala et a., 2019). The red dotted line indicates the position of DE.

545   B. Tissue annotation of gastrulation-stage mouse embryos with tissues expressing *Otx2*

546   listed. Arrows indicate different developmental trajectories along which *Otx2* is expressed.

547   C. Design of the murine OTX2-dTAG allele. Coordinates indicate the position of the *Otx2*

548   STOP codon (mm10), which was replaced with a multipurpose cassette. Blue box

549   indicates a linker peptide.

550   D. HA Western blotting (WB) after treatment of OTX2-dTAG EpiLC or EpiLCs derived from

551   parental wildtype (WT) mESCs with dTAG-13 or DMSO for the indicated periods of time.

552   Asterisk indicates a non-specific band.

553   E. Representative IF images after staining anterior micropatterns formed in presence (top)

554   or absence (bottom) of OTX2 for marker proteins of indicated lineages.

555   F.   Average marker intensity (+/- standard error of the mean) at different radial positions in

556   anterior micropatterns. N = colonies analyzed.

G. Protocol for directed differentiation of EpiSCs into DE, indicating compounds applied and timing of dTAG-13 administration for experiments shown in **Figs. 1I,J.**

H. Quantification of Otx2-EGFP levels at indicated stages of directed differentiation. Dotted line indicates level of background fluorescence measured in WT cells. (****)$p<0.0001$ with one-way ANOVA with Tukey's multiple comparison test.

I. Quantification by flow cytometry of $CXCR4^+PDGFRA^-$ (DE) and $PDGFRA^+CXCR4^-$ (mesoderm) cells following directed differentiation in control (DMSO) or OTX2-depleted (dTAG-13) conditions. (***)$p<0.001$ and (****)$p<0.0001$ with unpaired t-test. N=4 separate cultures from each of two independent cell lines.

J. Quantification of IF imaging of SOX17 (an endodermal marker) in DE derived from two independent OTX2-dTAG EpiSC lines cultured in absence or presence of dTAG-13. (****)$p<0.0001$ with unpaired t-test. N=4 separate cultures per cell line.

Figure 2. Transcriptional dysregulation in DE upon OTX2 depletion

A. Force-directed layout graph of scRNA-seq analyses on WT EpiSCs, DE treated with DMSO and DE treated with dTAG-13 at PS ($OTX2^{depl\_PS}$) DE cells.

B. Volcano plot showing expression changes (logFC) and statistical significance (padj) in $OTX2^{depl\_PS}$ DE with DEGs (logFC>1;padj<0.05) highlighted in blue (DEG^{DOWN}) and red (DEG^{UP}), respectively. DEGs highlighted in the text or in other figure panels are annotated.

C. Gene ontology (GO) analysis for DEG^{DOWN} and DEG^{UP} in $OTX2^{depl\_PS}$ DE using ENRICHR, listing top ranked GO terms for each gene category.

D. Normalized expression profiles of select DEG^{DOWN} (blue names) and DEG^{UP} (red names) in $OTX2^{depl\_PS}$ DE that associated with indicated cellular programs.

E. Comparison of the fold-change effect (dTAG-13:DMSO) on expression of select DEGs when OTX2 is depleted during (dTAG_PS; x-axis) or after (dTAG_DE; y-axis) DE specification. Genes DEGs only upon OTX2 depletion at PS are highlighted in red, all other genes are DEGs in both conditions.

F. Normalized expression levels of a panel of anterior-posterior gut tube markers (Pijuan-Sala et al., 2019) $OTX2^{depl\_PS}$ DE, $OTX2^{depl\_DE}$ DE and in control DE treated with DMSO.

G. Protocol to differentiate DE into $SOX2^+PDX1^+$ gastric foregut progenitors.

H. Quantification of SOX2$^+$PDX1$^+$ foregut clusters formed after OTX2 depletion at either PS or DE compared to cells differentiated in DMSO. (*)p<0.05 and (**)p<0.01 with one-way ANOVA and Kruskal-Wallis multiple comparison test.

Figure 3. Dynamics of OTX2 genome occupancy during DE specification

A. Classification and number of OTX2 binding sites identified by CUT&RUN in EpiSCs and DE.

B. GO analysis of genes in proximity of EPI, primed, and *de novo* OTX2 binding sites.

C. HOMER TF motif analysis at EPI, primed, and *de novo* OTX2 binding sites. The analysis was restricted to TFs expressed in DE and/or EpiSCs.

D. IGV tracks of OTX2 genome occupancy at select DEG^{DOWN} loci with examples of genes exhibiting primed (left two panels) or *de novo* (right two panels) OTX2 binding.

E. IGV tracks of OTX2 genome occupancy at select DEG^{UP} loci with examples of primed (top panel) and *de novo* (bottom panel) OTX2 binding.

F. Percentage of DEG^{DOWN}, DEG^{UP} and gene loci unaffected by OTX2 depletion ("unchanged") with OTX2 peaks of increasing (Q1 to Q4) intensity.

G. Distribution of DEG^{DOWN} gene loci with evidence of primed (site bound both in EpiSCs and DE) and *de novo* (site bound only in DE) OTX2 binding with example genes highlighted. Note that all gene loci with primed peaks also harbor additional *de novo* peaks but not vice versa.

H. Normalized expression levels of DEG^{DOWN} with either primed or *de novo* only OTX2 binding in EpiSCs, DE_DMSO an DE_dTAG. (****)p<0.0001 with two-sided unpaired Wilcoxon test.

Figure 4. OTX2-dependent remodeling of chromatin accessibility during DE specification

A. Volcano plot showing ATAC-seq signal in DMSO-treated DE versus DE treated with dTAG-13 at PS. Significantly different DARs (logFC>1;padj<0.05) are colored in blue (DAR^{DOWN}) and red (DAR^{UP}).

B. Four categories of DARs (C1-C4) identified by supervised clustering of ATAC-seq signal intensity in EpiSCs, control DE and OTX2-depleted DE.

20

618   C. Normalized expression levels of genes in vicinity of C1 to C4 DARs in indicated samples.
619   (***)p<0.001 and (****)p<0.0001 with two-sided unpaired Wilcoxon test.

620   D. Example of chromatin accessibility changes at DEG^{DOWN} loci representing major cellular
621   programs affected by OTX2.

622   E. Frequency and type of OTX2 binding at C1 to C4 DARs.

623   F. HOMER TF motif enrichment at C1-C4 DARs. Analysis was restricted to TFs expressed
624   in EpiSCs, DE, or both. Dotted lines indicate TFs exhibiting enrichment at similar DAR
625   categories.

626

627 **Figure 5. Impaired human DE formation upon OTX2 depletion**

628   A. Design of the human OTX2-dTAG allele. Coordinates indicate the position of the *Otx2*
629   STOP codon (in hg38) replaced with the multipurpose cassette. The blue box indicates a
630   linker peptide.

631   B. Anti-HA WB with OTX2-dTAG hESCs (n=3 lines) and parental cells after 1h of culture in
632   the presence of dTAG-v1 or DMSO. * = minor band indicating incomplete cleavage of
633   P2A fusion protein.

634   C. Representative flow cytometry plots showing CXCR4 and CD117 expression in human
635   DE derived from MEL-1 cells after culture in the presence of DMSO (top) or dTAG-v1
636   (bottom) from the PS stage onwards. Cells with a canonical DE cell surface phenotype
637   are highlighted.

638   D. Abundance of cells with the canonical DE phenotype (CXCR4^{+}CD117^{+}) in cultures
639   initiated with two independent OTX2-dTAG hESC lines and exposed to either DMSO or
640   dTAG-v1 in two different culture conditions (n=3 independent cultures). (***)p<0.001 or
641   (****)p<0.0001 with multiple T-tests and Bonferroni-Dunn correction.

642   E. Measurement by qPCR of effect of dTAG-v1 treatment on select human genes whose
643   mouse homologues are altered in their expression levels by OTX2 depletion in DE.
644   (*)p<0.05, (***)p<0.001 or (****)p<0.0001 with multiple T-tests and Bonferroni-Dunn
645   correction.

646   F. EGFP fluorescence levels in DE cultures established in either presence of DMSO or
647   dTAG-v1. Cultures established from parental non-transgenic (WT) human ESCs serve as
648   control for background fluorescence.

G. Representative low-magnification fluorescent live cell images of OTX2-EGFP+ human DE derived in presence of DMSO (top) or dTAG-v1 (bottom). Images are of MEL-1 derived cells using Protocol 1, but similar differences in cell clustering were observed with H9-derived cells and with DE generated using media 2.

H. Schematic highlighting major functions of OTX2 during mouse and human DE specification.

Figure S1. OTX2 depletion impairs DE development in murine models of germ layer specification

A. *In silico* strategy to identify candidate transcriptional regulators of germ layer specification from a recently assembled list of 1,682 TFs encoded in the mouse genome (Garipler et al., 2022).

B. *Otx2* expression levels in DE and in tissues with known *Otx2* functions (visceral endoderm, rostral neuroectoderm) present in gastrulation-stage mouse embryos (Pijuan-Sala et al., 2019). Extra-embryonic endoderm (ExE endoderm) and PGCs are shown as representative tissues not expressing *Otx2*.

C. Percentage Otx2-EGFP+ cells in cultures of mESCs, EpiLCs and EpiSCs as measured by flow cytometry. (**) p<0.01 with two-way ANOVA with Tukey's multiple comparison test (n=3 independent cultures).

D. Experimental strategy for the generation of anterior micropatterns ("gastruloids") with timing of dTAG-13 treatment indicated.

E. IF quantification of intensity of stage-specific marker proteins at indicated stages of differentiation. (****) p<0.0001 with one-way ANOVA with Tukey's multiple comparison test. N > 500 nuclei were analyzed for each marker and sample.

F. Quantification of OTX2 (via HA IF) in PS cultures after 1h of exposure to dTAG-13 or DMSO. (****) p<0.0001 with one-way ANOVA with Tukey's multiple comparison test. N > 500 nuclei were analyzed for each marker and sample.

G. Representative flow cytometry plots showing CXCR4 (endoderm marker) and PDGFRA (mesoderm marker) expression in DE established from OTX2-dTAG EpiSCs and EpiSCs derived from parental wildtype (WT) mESCs in presence of DMSO (top panels) or dTAG-13 (bottom panels).

22

H. IF quantification of intensity of SOX17 protein in DE established from WT EpiSCs cultured in presence of DMSO or dTAG-13. Statistics with unpaired t-test.

I. Ratio of CXCR4 levels in presence of DMSO or dTAG-13 as measured by flow cytometry on OTX2-dTAG (KI) and WT DE in mixed cultures of the indicated ratios. OTX2-dTAG were distinguished from WT cells based on EGFP expression.

Figure S2. Figure 2. Transcriptional dysregulation in DE upon OTX2 depletion

A. Expression levels of select genes not affected by OTX2 depletion, including a subset of DE markers (*CD24a*, *Hhex*, *Larp7*) as well as markers for visceral endoderm (*Sox7*), primitive endoderm (*Ttr*), cell cycle progression (*Aurka*, *Plk1*) and primed pluripotency (*Sox2*, *Nanog*, *Pou3f1*).

B. Abundance of cells assigned an "Epi", "DE" or altered DE ("DE_alt") identity in indicated cultures based on scRNA-seq analysis.

C. Expression levels of select DEG^{DOWN} (blue) and DEG^{UP} (red) after OTX2 depletion at PS, representing developmental TFs, signaling regulators and proteins involved in cellular adhesion or migration.

D. Expression in gastrulation-stage embryos (from Pijuan-Sala et a., 2019) of select TFs associated with indicated non-DE lineages that are upregulated in DE upon OTX2 depletion. The red outline indicates position of DE in the embryonic UMAP.

E. Correlation between expression levels of *Sox17* (DE marker) and levels of indicated non-DE markers in DE cultures established in presence of DMSO (left panels) or dTAG-13 (right panels).

F. Validation by qPCR of the effect of OTX2 depletion on select DEG^{DOWN} (blue) and DEG^{UP} (red) in two independent cell lines. (*) $p<0.05$, (**) $p<0.01$, (***) $p<0.001$ and (****) $p<0.0001$ with multiple t-tests and Bonferroni-Dunn correction. N = 3 measurements.

G. Volcano plot showing expression changes in $OTX2^{depl\_DE}$ DE with DEGs (logFC>1;padj<0.05) in blue (DOWN) or red (RED), respectively.

H. Representative IF images after staining of gastral foregut cultures exposed to DMSO or dTAG-13 at PS or DE with SOX2 and PDX1 antibodies.

Figure S3. Dynamics of OTX2 genome occupancy during DE specification

23

A. Tornado plot showing signal intensity at HA CUT&RUN peaks called in OTX2-dTAG EpiSCs and DE as well as in corresponding genomic regions in WT (non-transgenic) DE.

B. Cell-type specific (EpiSCs and DE) HA CUT&RUN intensity at EPI, primed and *de novo* OTX2 peaks. (****)p<0.0001 with paired Wilcoxon test.

C. Genomic distribution of EPI, primed and *de novo* HA CUT&RUN peaks.

D. IGV tracks showing cell type-specific OTX2 binding at the pluripotency-associated *Pou5f1* locus, a known target of OTX2 in primed pluripotent cells.

E. Fraction of DEG^{DOWN}, DEG^{UP} and control genes unaffected by OTX2 depletion that have an associated OTX2 peak in DE.

F. Average number of OTX2 peaks (in DE) at OTX2 bound DEG^{DOWN} (n=327), DEG^{UP} (n=345) and unaffected gene loci (n=572). (****)p<0.0001 with Mann-Whitney test for unpaired data, two side and confidence interval of 95%.

G. Intensity of HA CUT&RUN signal at promoter and non-promoter OTX2 peaks associated with DEG^{DOWN} (n=360 for promoters; n=942 for non-promoters), DEG^{UP} (n=344 for promoters; n=915 for non-promoters) and unaffected control genes (n=451 for promoters; n=752 for non-promoters). (*)p<0.05, (**)p<0.01 and (****)p<0.0001 with Mann-Whitney test for unpaired data, two side and confidence interval of 95%.

H. Overlap of OTX2-bound DEG^{DOWN} (top) and DEG^{UP} (down) gene loci with primed OTX2 peaks (green) and such loci with *de novo* OTX2 peaks (blue).

Figure S4. OTX2-dependent remodeling of chromatin accessibility during DE specification

A. Percentage of genomic regions with differential chromatin accessibility between EpiSCs (Medina-Cano et al., 2022) and DE that are bound by OTX2 in either, both or neither cell type.

B. MA plot showing ATAC-seq signal change in DE derived in either presence of DMSO or dTAG-13. Significantly different (logFC>1;padj<0.05) DARs are indicated in red (UP) or blue (DOWN).

C. Fraction of regions that change their chromatin accessibility in DE upon OTX2 depletion (DARs DMSO vs dTAG) that undergo accessibility changes during the transition from EpiSCs to DE (green) or not (yellow).

24

D. Genomic distribution of genomics regions in DE that are affected in their chromatin accessibility by OTX2 depletion at PS (C1 to C4).

E. Fraction of DEG^{DOWN}, DEG^{UP} and unaffected control genes with an associated C1-C4 DAR or no associated DAR.

F. Intensity of HA CUT&RUN signal at C1 to C4 DARs in EpiSCs (top) and DE (bottom). Wilcoxon test was used for statistics (each group versus the ensemble of peaks per cell type) with (****)$p<0.0001$.

G. Supervised clustering of TF motif enrichment at C1-C4 DARs, distinguishing between DARs bound by OTX2 and DARs not bound by OTX2. Dotted lines indicate TFs exhibiting enrichment at similar DAR categories.

H.

Figure S5. Impaired human DE formation upon OTX2 depletion

A. Select DE-associated TFs ranked by their degree of protein conservation between mouse and human.

B. Anti-HA IF of OTX2-dTAG hESCs exposed to either DMSO, dTAG-v1 or dTAG-13 for 2h. Parental hESCs cultured in DMSO are shown to represent background fluorescence levels. Note residual retention of HA signal in presence of dTAG-13.

C. Outline of the two differentiation regimens for the generation of DE from hESCs employed in this study. Differences in compounds used or concentrations applied are highlighted in red.

D. Percentage of OTX2-EGFP$^+$ cells in OTX2-dTAG hESCs and derivative DE.

E. OTX2-EGFP expression levels (as measured by flow cytometry) in hESCs an DE (derived in two different media compositions) of indicated backgrounds. The grey dotted line indicates background fluorescence levels measured in parental, non-transgenic hESCs. (***) $p<0.001$ and (****) $p<0.0001$ with one-way ANOVA with Tukey's multiple comparison test.

F. Representative IF images after staining human DE derived in either presence of dTAG-v1 or DMSO with anti-SOX17 antibody or DAPI.

25

773 **Tables with titles and legends**

774 Table S1. Expression levels of TFs in EpiLCs and mESCs

775 Table S2. DEGs identified by scRNA-seq

776 Table S3. List of OTX2 peaks identified by HA CUT&RUN

777 Table S4. List of DARs identified by ATAC-seq

778 Table S5. List of DNA oligos used in this study

779

780

781

782 **Resource availability**

783 **Lead Contact**

784 Requests for resources and reagents should be directed to and will be fulfilled by the lead

785 contact, Matthias Stadtfeld (mas4011@med.cornell.edu).

786

787 **Materials availability**

788 Cell lines generated in this study are available upon request from the lead contact.

789

790 **Data and code availability**

791 CUT&RUN, scRNA-seq and ATAC-seq data have been deposited at Gene Expression Omnibus

792 (GEO) with accession codes: GSE254428, GSE254431 and GSE254590, respectively. The

793 deposited data will be publicly available as of the publication date.

794

795

796 **Experimental model and subject details**

797

798 **Mouse cell lines**

799 Parental mouse ESC lines used for gene targeting were KH2 (Beard et al., 2006) or 5.8 (Zhong

800 et al., 2023), both on a C57BL/6J x 129S1 F1 background. OTX2-dTAG mESCs were generated

801 using CRISPR/Cas9. Homology arms covering 778bp upstream and 680bp downstream of the

802 *Otx2* C-terminus were PCR-amplified from genomic DNA and cloned with the FKBP12^{F36V}-

803 2xHA-P2A-NLS-EGFP construct into pBluescript (Stratagene) using Gibson assembly. The

26

804 OTX2-FKBP12^{F36V}-2xHA-P2A-NLS-EGFP targeting vector was transfected into the

805 abovementioned ESC lines along with pX330-puro^R or -blasticidin^R vector harboring guide RNAs

806 targeting the *Otx2* C-terminus. 2 x 10^5 ESCs were cultured overnight and transfected with 3μg

807 of each plasmid using TransIT-293 (Mirus Bio 2700). Cells were replated at low density onto

808 10cm dishes with the corresponding antibiotic selection for 24-72 hours. Individual clones were

809 screened by PCR followed by TOPO cloning (Invitrogen) and sequencing.

810

811 **Mouse ESC culture and epiblast conversion**

812 ESCs were cultured in KO DMEM (Gibco 10829018) supplemented with 15% FBS (Gemini

813 Benchmark), 2mM Glutamax (Gibco 35050079), 0.1mM nonessential amino acids (Gibco

814 11140076), 0.1mM 2-mercaptoethanol (Gibco 21985023), 1000U/ml leukemia inhibitory factor

815 (LIF; in house), and 100μg/ml penicillin/streptomycin (Gibco 15140163) and maintained on a

816 feeder layer of mitomycin C-treated mouse embryonic fibroblasts (MEFs) on gelatin-coated

817 plates. For ESC to EpiLC conversion, ESCs were lifted using collagenase IV (Thermo Fisher

818 17104019), centrifuged for 4min at 120g, and dissociated with Accutase (Thermo Fisher

819 00455556). 15,000 cells/cm^2 were seeded onto fibronectin (Millipore FC010; 16.7ug/ml)-coated

820 plates in N2B27 media with 12.5ng/ml heat stable bFGF (Thermo PHG0360) and 20ng/ml Activin

821 A (Peprotech 120-14P) (FA media) supplemented with 1% Knockout Serum Replacement

822 (Gibco 10828010). EpiLCs were harvested or converted to EpiSCs after 48hrs differentiation.

823 For EpiSC conversion EpiLCs were dissociated with TrypLE (Thermo Fisher 12605010) and

824 plated onto gelatin-coated plates with feeders at 15,000 cells/cm^2 in EpiSC media (FA

825 supplemented with 175nM NVP-TNKS656 (Selleck S7238).

826

827 **Mouse definitive endoderm specification and foregut conversion**

828 EpiSCs cultured between passages 2-7 were differentiated first to primitive streak/

829 endomesodermal progenitors (PS) and then to definitive endoderm (DE) as described (Medina-

830 Cano et al., 2022). Briefly, EpiSCs were seeded onto 96, 48, or 24well plates coated with

831 10ug/ml Laminin 521 (StemCell Technologies 77003) in plating media. Plating media (chemically

832 defined media, CDM) is 1:1 IMDM (Gibco 12440053) and DMEM/F12 with Glutamax (Gibco

833 10565018), 1% chemically defined lipid concentrate (Thermo Fisher 11905031),

834 monothioglycerol (Sigma M6145), Apotransferrin (R&D 3188AT), 0.7 μg/ml insulin (Millipore

835 Sigma I0516), and polyvinyl alcohol (Sigma P8136) supplemented with 12.5ng/ml bFGF,

836 20ng/ml activin A, 175nM NVP, 1% KSR and 2 μM thiazovivin (Millipore Sigma SML1045). PS

837 was induced 5-6 hours after seeding with CDM + 40ng/ml activin A and 3μM CHIR99021

838 (Biovision 16775). DE was induced 16 hours after PS with CDM + 100ng/ml activin A and 100nM

839 LDN193189 (Reprocell 04-0074). Cells were washed 1x in PBS -/- between all media changes.

840 To convert DE to antral gastric progenitors (posterior foregut), DE cultured for 48 hours was

841 grown for an additional 48 hours in CDM with 100nM LDN193189 and 2% FBS. 2μM retinoic

842 acid was added, and cells cultured for 24 hours before fixation and staining. Cells were treated

843 with 500nM dTAG13 (Tocris 6605) in DMSO or vehicle control in culture media at the indicated

844 amounts of time.

845

846 **Micropatterns**

847 ESCs were converted to EpiLCs for 48hrs and seeded onto micropattern chips (CYTOO Arena

848 A) as described (Morgani and Hadjantonakis, 2021). Briefly, 2-6 x 10^6 EpiLCs were plated in

849 EpiLC media onto micropattern chips coated with 10μg/ml Laminin 521. Media was replaced

850 with FA after 2h and cells allowed to aggregate on micropatterns for 24hrs. 200 ng/ml Wnt3a

851 (R&D 5036-WNP) was added to induce anterior differentiation. Chips were fixed and stained

852 48hrs after Wnt3a addition.

853

854 **Human ESC culture and genetic engineering DE conversion**

855 Human MEL-1 and H9 ESCs were cultured on tissue culture plates coated with vitronectin (5

856 μg/ml) in Essential 8 Flex media with supplements and normocin (50 μg/ml) ("E8"). Cells were

857 passaged with home-made EDTA Dissociation Solution (0.5 mM EDTA and 35 mM NaCl in PBS)

858 during maintenance or with Accutase for freezing or when preparing single cell suspensions.

859 Cells were frozen in Stem Cell Banker. After thawing, Y-27632 was added at 10 μM to the culture

860 media for 24 hours. A targeting vector for generation of the human OTX2-dTAG allele was built

861 by combining a 1252bp PCR amplicon (chr14:56,801,072-56,802,323 in hg38) generated from

862 MEL-1 genomic DNA with a FKBPV-2xHA-P2A-NLS-EGFP cassette, using Gibson assembly.

863 The resulting vector was introduced into MEL-1 and H9 hESCs together with the pX330 Cas9

864 vector expression a guide RNA (5'-GTACAGGTCTTCACAAAACC-3') targeting the *OTX2* STOP

865 codon using lipofection in mTeSR media mixed with CloneR solution (1:10). Transfected cells

866 were selected for 48h with G418 (500 µg/ml), using mTeSR:CloneR (1:10). After selection, cells

867 were seeded at clonal density and grown in E8 supplemented with CloneR (1:10) for three days

868 and another five days in E8 without CloneR when colonies with undifferentiated morphology and

869 homogenous nuclear EGFP fluorescence were picked. Clonal lines were expanded and

870 characterized by flow cytometry (intensity and homogeneity of EGFP fluorescence), genotyping

871 PCR (using the primers 5'-GGCAGGGGAAATTGTGTGTT-3' and 5'-

872 TCGTAAAGTTTCAGTGCAGCT-3' which localize on either side outside of the *OTX2* homology

873 region included in the targeting vector), by Sanger sequencing of the PCR amplicon and by IF

874 using antibodies against HA and OTX2. Confirmed homozygous lines were karyotyped before

875 use in differentiation experiments.

876

Human DE specification

878 Single cell suspensions of hESCs were seeded in E8 supplemented with 10 µM Y-27632 onto

879 cell culture vessel that were coated with Laminin-521 at 4°C for 24h to achieve a seeding density

880 of 30-40%. The next day, cells were washed with prewarmed F12 based media and cultured for

881 24h in PS induction media Cells were then washed with prewarmed F12 based media and

882 cultured for another 40h to 48h in DE induction media, with one media change after 24h of

883 culture. Two protocols slightly differing in their use of signaling modulators were used. Protocol

884 1 uses the same PS and DE induction media applied to mouse DE. Protocol 2 uses PS induction

885 media with 100 ng/ml Activin A, 2 µM CHIR99021 and 100 mM PIK90 (Selleckchem S1187) and

886 DE induction media with 250 nM LDN1931189 (see also Fig. S5C). Both protocols use identical

887 base media and overall experimental timing.

888

Immunofluorescence

890 For micropatterns, chips were washed 2x in PBS -/-, fixed in 4% PFA for 15min, and washed

891 again 2x in PBS -/-. Chips were stained as described [ref]. Primary antibodies used were rat anti-

892 SOX2 (), goat anti-SOX17 (), and rabbit anti-FOXA2 (Abcam), all at 1:300. Secondary antibodies

893 (Alexa Fluor, Life Technologies, and Jackson Immunoresearch) were used at 1:500.

894 Micropattern chips were mounted on microscope slides with Fluoromount G (Thermo Fisher

895 00495802) and imaged on an LSM880 confocal microscope (Zeiss). For EpiSCs, DE and

896 foregut, cells were washed and fixed in wells as above, blocked in PBS +/+ with 1% BSA, 0.1%

897 Triton-X-100, and 3% donkey serum (Sigma D9663) and stained in primary antibodies overnight.
898 Cells were washed 3x in PBS +/+ with 0.1% Triton X-100 (PBS-T) and then incubated in
899 secondary antibodies for 1 hour. Cells were then again washed 3x in PBS-T. Hoechst33342
900 (Thermo Fisher H3570) was added to the last wash for 15 minutes for nuclear staining. Images
901 were taken on an EVOS Cell Imaging System (Thermo Fisher) or Leica DMi8 microscope.
902 Primary antibodies used were anti-SOX17 (R&D AF1924), anti-FOXA2 (Abcam 108422), anti-T
903 (R&D AF2085), anti-HA (Abcam 9110) anti-OCT4 (Santa Cruz 8628), anti-GFP (Aves
904 GFP1020), anti-SOX2 (Invitrogen 14981180), anti-PDX1 (Abcam 47308). For both
905 micropatterns and directed differentiation, primary antibodies were used at 1:300 except anti-
906 HA and anti-GFP (1:1000) and anti-PDX1 (1:100). Secondary antibodies (Alexa Fluor, Life
907 Technologies, and Jackson Immunoresearch) were used at 1:500.

908

909 **Flow cytometry**
910 Cells were washed with PBS -/-, dissociated with Accutase, resuspended in FACS buffer (80%
911 PBS -/-, 20% FBS, 0.1% 0.5M EDTA), and incubated with indicated antibodies for 15min at room
912 temperature in the dark. Cells were washed once in PBS -/-, resuspended in FACS buffer with
913 DAPI, and analyzed on a BD FACS Canto. Data were analyzed using FlowJo. CXCR4 antibody
914 conjugated to APC (eBioscience 17999182) and PDGFRa antibody conjugated to PE-Cy7
915 (eBioscience 25140180) were used at 1:200 dilution.

916

917 **RT-qPCR**
918 Total RNA was extracted using TRIzol (Life Technologies 15596018) and purified with the RNA
919 Clean and Concentrator kit (Zymo R1014). 1µg of RNA/sample was used for reverse
920 transcription using the iScript kit (BioRad 1708841). qPCR was performed on cDNA samples in
921 triplicate using PowerUp SYBR green PCR master mix (Thermo Fisher A25778) on an Applied
922 Biosystems QuantStudio3. Primers used are in **Table S5**.

923

924 **Western blotting**
925 Cells were washed with PBS -/- and harvested with Trypsin (Life Technologies 25200114).
926 Nuclear lysates were prepared using the NE-PER kit (Thermo Fisher 78835) according to the
927 manufacturer's instructions. Western blots were performed using the following antibodies: anti-

30

928   HA (Abcam 9110), anti-OTX2 (Abcam 21990), anti-histone H3 (Abcam 1791). Protein

929   concentration was measured using Bradford Reagent (BioRad 5000201) and samples were

930   boiled, resuspended in Laemmli Sample Buffer (BioRad), and run using BioRad PROTEAN

931   System or Invitrogen precast gels.

932

933   **scRNA-seq**

934   Cells at indicated stages were dissociated using Accutase to single-cell suspension in PBS-/-

935   with 0.04% BSA. Samples were labeled with Cell Multiplexing Oligos (10x Genomics Chromium

936   Next GEM Single Cell 3′ Reagent Kit v3.1 Dual Index) and live cells sorted using DAPI on a BD

937   Influx Cell Sorter. Samples were then pooled for multiplexing in PBS-/- with 0.04% BSA

938   (targeting 10,000 cells/sample) and single-cell libraries generated according to the

939   manufacturer's instructions (10x Genomics Chromium Single Cell Gene Expression - Cell

940   Multiplexing). All cell sorts and deep sequencing were performed at the Weill Cornell Flow

941   Cytometry and Weill Cornell Genomics Resources Core Facilities respectively.

942

943   **CUT&RUN**

944   CUT&RUN on OTX2-HA was performed on 500,000 EpiSCs or DE cells, similar as previously

945   described (Skene et al., 2018). For DE, live cells were selected by DAPI sort on an Influx Cell

946   Sorter before performing CUT&RUN. BioMag Plus Concanavalin A beads (ConA beads,

947   PolySciences NC1358578) were washed twice in 100μl cold Bead Activation Buffer (20mM

948   HEPES pH7.5, 10mM KCl, 1mM CaCl$_2$, 1mM MnCl$_2$). 20μg of ConA beads per CUT&RUN

949   reaction were used. Sorted cells were washed twice in Wash Buffer (20mM HEPES pH7.5,

950   150mM NaCl, 0.5mM Spermidine (Acros AC132740050), ½ Protease Inhibitor tablet) and bound

951   to activated ConA beads in Wash Buffer for 10 minutes at room temperature. Samples were

952   incubated in PCR strip tubes with 1:100 anti-HA (CST C29F4 #3724) or anti-IgG (EpiCypher

953   130042) in Antibody Buffer (Wash Buffer with 2mM EDTA and 0.01% Digitonin (Millipore Sigma

954   300410)) overnight with gentle rocking at 4°C. Samples were washed twice in Digitonin Buffer

955   (Washer Buffer with 0.01% Digitonin) and ProteinA/G MNase (EpiCypher) was bound to samples

956   for 1 hour at 4°C. ProteinA/G MNase was diluted at 20x in 50μl Antibody Buffer according to

957   manufacturer's instructions. Samples were washed twice in Digitonin Buffer again and MNase

958   digestion was activated with 1μl 100mM CaCl$_2$ in 50μl Digitonin Buffer for 2 hours. To extract

31

959 bound chromatin fragments digestion was quenched using 33μl STOP Buffer (340mM NaCl,

960 20mM EDTA, 4mM EGTA, 50μg/ml RNAse A, 50μg/ml glycogen, 0.015 ng/μl E. coli spike-in)

961 and samples incubated at 37°C for 20 minutes. Chromatin was separated from ConA beads by

962 centrifuging 5 minutes at 16,000g and saving supernatant. DNA was purified by adding 0.1%

963 SDS and 5μg Proteinase K for 10 min at 70°C, performing phenol-chloroform extraction, and

964 precipitation in 100% ethanol at -80°C overnight. Pellets were then washed in 100% ethanol and

965 resuspended in 12μl nuclease free water. CUT&RUN libraries were prepared using the Thruplex

966 Library Prep kit (Takara) according to the manufacturer's instructions. The number of cycles for

967 library PCR amplification was determined by running 10% of each library sample in an Applied

968 Biosystems qPCR machine with 0.25μl Eva Green dye (Biotium 31000) for 40 cycles and adding

969 cycles to each sample as described (Buenrostro et al., 2015). Libraries were size selected with

970 1.5x volume SPRI beads (Beckman Coulter B23317) and sequenced at the Weill Cornell

971 Genomics Resources Core Facility on an Illumina NovaSeq 6000 (PE-50, 30 million reads per

972 sample).

973

974 **ATAC-seq**

975 DE cultured with dTAG13 or DMSO vehicle for 24 hours was sorted for live cells on Influx as

976 described for CUT&RUN. ATAC-seq was performed on three technical replicates of 50,000 cells

977 each for DMSO or dTAG13-treated cultures as described (Murphy et al., 2023) using the Nextera

978 DNA library preparation kit (Illumina FC121103) and NEBNext High-Fidelity 2X PCR Master Mix

979 (NEB M0541). Libraries were sequenced on an Illumina NovaSeq 6000 (PE-50, 20 million reads

980 per sample).

981

982 **Data analysis**

983 **scRNA-seq analysis**

984 Fastq files were processed using CellRanger (10x genomics cloud). The raw h5 file was further

985 processed using CellBender to eliminate background reads, empty beads, and other artifacts

986 (Fleming et al., 2022). Scanpy (Wolf et al., 2018) was used for downstream analyses. Only cells

987 efficiently labeled with the demultiplexing primers were kept. Resulting cell clusters with high

988 percentage of mitochondrial reads or a relatively low number of reads were eliminated. Palantir

989 (Setty et al., 2019) was used for pseudo-time analyses. For differential expression analyses,

32

990 Wilcoxon testing was performed and only genes with padj<0.05 and log2 fold-change>1 were

991 considered as differentially expressed genes (DEGs). The scores/ranking per gene given by the

992 scanpy.get.rank_genes_groups_df function were used.

993

994 **CUT&RUN sequencing analysis**

995 CUT&RUN fastq files were processed as previously described (Uyehara et al., 2022) using a

996 custom snakemake (v6.6.1) pipeline (Molder et al., 2021). Briefly, reads were trimmed using

997 bbmap (v38.95) with parameters ktrim=r ref=adapters rcomp=t tpe=t tbo=t hdist=1 mink=11.

998 Trimmed reads were aligned to the mm10 reference genome using Bowtie2 (v2.3.5.1) with

999 parameters --local --very-sensitive-local --no-mixed --no-discordant --phred33 -I 5 -X 999

1000 (Langmead and Salzberg, 2012). Reads with a MAPQ score less than 5 were removed with

1001 samtools (v1.14) (Li et al., 2009). PCR duplicates were removed with Picard (v2.26.10) using

1002 parameter VALIDATION_STRINGENCY=LENIENT. Fragments between 20 and 120bp were

1003 isolated using a custom awk script and used for downstream analyses as previously

1004 recommended (Skene and Henikoff, 2017). Bigwigs were generated from bam files using

1005 bedtools (v2.30) normalizing to sequencing depth using the formula: (effective_genome_size /

1006 read_count * read_length) with 1870000000 as the effective genome size (Quinlan and Hall,

1007 2010). Bam files were converted to bed files with bedtools (v2.30) with parameter -bedpe. MACS

1008 (v2.2.6) was used to call peaks on individual and merged replicates using parameters -g

1009 1870000000 --nomodel --seed 123 –keep-dup all (Zhang et al., 2008).

1010

1011 **ATAC-seq**

1012 The raw ATAC-seq reads were trimmed using fastp to remove low-quality bases from reads

1013 (quality<20) and adapter sequences. The trimmed reads were aligned using Bowtie2 (Langmead

1014 and Salzberg, 2012) to UCSC genome assembly mm10. Duplicate reads were removed using

1015 Sambamba. Peaks were identified with MACS2 (Gaspar, 2018) and those overlapping with

1016 satellite repeat regions were discarded. For further analyses, a union peak atlas was created

1017 from the MACS2 files. Peak intensity for each sample was counted using featureCounts (Liao et

1018 al., 2014). HOMER (v4.11) (Heinz et al., 2010) was used for motif analyses. To associate peaks

1019 with nearby genes and genomic location, ChipSeeker (Yu et al., 2015) was used. To compare

1020 peaks from CUT&RUN and ATAC-seq experiments, *bedtools intersect* (Quinlan and Hall, 2010)

1021 was used with default parameters. The dataset published by (Medina-Cano et al., 2022) was

1022 used as a reference EpiSC dataset.

1023

Quantification and statistical analyses

1025 Statistical analysis of flow cytometry and IF data was done in PRISM 9 (GraphPad), with specific

1026 tests and corrections applied indicated in the respective figure legends.

1027

Image analysis

1029 Immunofluorescence images were analyzed using Fiji/ImageJ (Schindelin et al., 2012). For

1030 directed differentiations, fluorescence intensity was quantified using CellProfiler 4.2.1 (Carpenter

1031 et al., 2006). Cells were identified by DAPI staining using the IdentifyPrimayObjects module and

1032 mean fluorescence intensity in each stained channel was measured using the

1033 MeasureObjectIntensity module. Statistical significance was calculated in PRISM 9 (GraphPad)

1034 using one-way ANOVA. For micropatterns, entire chips were imaged using a 5x objective and

1035 11x11 tiling. Individual colonies were detected based on DAPI, size and circularity thresholds

1036 using custom Fiji macros. The mean pixel intensity for each fluorescent channel for each colony

1037 as well as the mean and standard error across all colonies was calculated in MATLAB R2021a

1038 (MathWorks) and normalized by the maximum value from each channel using custom scripts

1039 (available upon request). For quantification of posterior foregut progenitors, $SOX2^+PDX1^+$ cell

1040 clusters on 24- or 48 well cell culture plates were imaged and counted at 10X magnification on

1041 a Leica DMi8 microscope. Cell clusters were quantified for 5 replicates per condition (dTAG-13

1042 added at PS or after 24 hours DE differentiation; and DMSO control). Cluster counts for each

1043 replicate were divided by the respective growth area (cm^2) to normalize for plate well area over

1044 two independent experiments. Significance was calculated using the Kruskal-Wallis

1045 nonparametric test.

1046

1047

1048

1049

1050

1051

34

References

Abuhashem, A., Lee, A.S., Joyner, A.L., and Hadjantonakis, A.K. (2022). Rapid and efficient degradation of endogenous proteins in vivo identifies stage-specific roles of RNA Pol II pausing in mammalian development. Dev Cell *57*, 1068-1080 e1066.

Acampora, D., Di Giovannantonio, L.G., and Simeone, A. (2013). Otx2 is an intrinsic determinant of the embryonic stem cell state and is required for transition to a stable epiblast stem cell condition. Development *140*, 43-55.

Acampora, D., Mazan, S., Lallemand, Y., Avantaggiato, V., Maury, M., Simeone, A., and Brulet, P. (1995). Forebrain and midbrain regions are deleted in Otx2-/- mutants due to a defective anterior neuroectoderm specification during gastrulation. Development *121*, 3279-3290.

Alexander, T.B., Gu, Z., Iacobucci, I., Dickerson, K., Choi, J.K., Xu, B., Payne-Turner, D., Yoshihara, H., Loh, M.L., Horan, J.*, et al.* (2018). The genetic basis and cell of origin of mixed phenotype acute leukaemia. Nature *562*, 373-379.

Ang, S.L., Jin, O., Rhinn, M., Daigle, N., Stevenson, L., and Rossant, J. (1996). A targeted mouse Otx2 mutation leads to severe defects in gastrulation and formation of axial mesoderm and to deletion of rostral brain. Development *122*, 243-252.

Arnold, S.J., Hofmann, U.K., Bikoff, E.K., and Robertson, E.J. (2008). Pivotal roles for eomesodermin during axis formation, epithelium-to-mesenchyme transition and endoderm specification in the mouse. Development *135*, 501-511.

Bardot, E.S., and Hadjantonakis, A.K. (2020). Mouse gastrulation: Coordination of tissue patterning, specification and diversification of cell fate. Mech Dev *163*, 103617.

Beard, C., Hochedlinger, K., Plath, K., Wutz, A., and Jaenisch, R. (2006). Efficient method to generate single-copy transgenic mice by site-specific integration in embryonic stem cells. Genesis *44*, 23-28.

Beby, F., and Lamonerie, T. (2013). The homeobox gene Otx2 in development and disease. Exp Eye Res *111*, 9-16.

Bernardo, A.S., Faial, T., Gardner, L., Niakan, K.K., Ortmann, D., Senner, C.E., Callery, E.M., Trotter, M.W., Hemberger, M., Smith, J.C.*, et al.* (2011). BRACHYURY and CDX2 mediate BMP-induced differentiation of human and mouse pluripotent stem cells into embryonic and extraembryonic lineages. Cell Stem Cell *9*, 144-155.

Bisia, A.M., Costello, I., Xypolita, M.E., Harland, L.T.G., Kurbel, P.J., Bikoff, E.K., and Robertson, E.J. (2023). A degron-based approach to manipulate Eomes functions in the context of the developing mouse embryo. Proc Natl Acad Sci U S A *120*, e2311946120.

Buecker, C., Srinivasan, R., Wu, Z., Calo, E., Acampora, D., Faial, T., Simeone, A., Tan, M., Swigut, T., and Wysocka, J. (2014). Reorganization of enhancer patterns in transition from naive to primed pluripotency. Cell Stem Cell *14*, 838-853.

Buenrostro, J.D., Wu, B., Chang, H.Y., and Greenleaf, W.J. (2015). ATAC-seq: A Method for Assaying Chromatin Accessibility Genome-Wide. Curr Protoc Mol Biol *109*, 21 29 21-21 29 29.

Bult, C.J., Blake, J.A., Smith, C.L., Kadin, J.A., Richardson, J.E., and Mouse Genome Database, G. (2019). Mouse Genome Database (MGD) 2019. Nucleic Acids Res *47*, D801-D806.

Carpenter, A.E., Jones, T.R., Lamprecht, M.R., Clarke, C., Kang, I.H., Friman, O., Guertin, D.A., Chang, J.H., Lindquist, R.A., Moffat, J.*, et al.* (2006). CellProfiler: image analysis software for identifying and quantifying cell phenotypes. Genome Biol *7*, R100.

Chia, C.Y., Madrigal, P., Denil, S., Martinez, I., Garcia-Bernardo, J., El-Khairi, R., Chhatriwala, M., Shepherd, M.H., Hattersley, A.T., Dunn, N.R.*, et al.* (2019). GATA6 Cooperates with EOMES/SMAD2/3 to Deploy the Gene Regulatory Network Governing Human Definitive Endoderm and Pancreas Formation. Stem Cell Reports *12*, 57-70.

1098 Cui, G., Suo, S., Wang, R., Qian, Y., Han, J.J., Peng, G., Tam, P.P.L., and Jing, N. (2018). Mouse
1099 gastrulation: Attributes of transcription factor regulatory network for epiblast patterning. Dev Growth
1100 Differ *60*, 463-472.
1101 Cunningham, F., Allen, J.E., Allen, J., Alvarez-Jarreta, J., Amode, M.R., Armean, I.M., Austine-Orimoloye,
1102 O., Azov, A.G., Barnes, I., Bennett, R.*, et al.* (2022). Ensembl 2022. Nucleic Acids Res *50*, D988-D995.
1103 Di Giovannantonio, L.G., Acampora, D., Omodei, D., Nigro, V., Barba, P., Barbieri, E., Chambers, I., and
1104 Simeone, A. (2021). Direct repression of Nanog and Oct4 by OTX2 modulates the contribution of
1105 epiblast-derived cells to germline and somatic lineage. Development *148*.
1106 Doane, A.S., Chu, C.S., Di Giammartino, D.C., Rivas, M.A., Hellmuth, J.C., Jiang, Y., Yusufova, N., Alonso,
1107 A., Roeder, R.G., Apostolou, E.*, et al.* (2021). OCT2 pre-positioning facilitates cell fate transition and
1108 chromatin architecture changes in humoral immunity. Nat Immunol *22*, 1327-1340.
1109 Drukker, M., Tang, C., Ardehali, R., Rinkevich, Y., Seita, J., Lee, A.S., Mosley, A.R., Weissman, I.L., and
1110 Soen, Y. (2012). Isolation of primitive endoderm, mesoderm, vascular endothelial and trophoblast
1111 progenitors from human pluripotent stem cells. Nat Biotechnol *30*, 531-542.
1112 Fleming, S.J., Chaffin, M.D., Arduini, A., Akkad, A.-D., Banks, E., Marioni, J.C., Philippakis, A.A., Ellinor,
1113 P.T., and Babadi, M. (2022). Unsupervised removal of systematic background noise from droplet-based
1114 single-cell experiments using <kbd>CellBender</kbd>. bioRxiv.
1115 Gaertner, B., Carrano, A.C., and Sander, M. (2019). Human stem cell models: lessons for pancreatic
1116 development and disease. Genes Dev *33*, 1475-1490.
1117 Garipler, G., Lu, C., Morrissey, A., Lopez-Zepeda, L.S., Pei, Y., Vidal, S.E., Zen Petisco Fiore, A.P., Aydin, B.,
1118 Stadtfeld, M., Ohler, U.*, et al.* (2022). The BTB transcription factors ZBTB11 and ZFP131 maintain
1119 pluripotency by repressing pro-differentiation genes. Cell Rep *38*, 110524.
1120 Gaspar, J.M. (2018). Improved peak-calling with MACS2. bioRxiv, 496521.
1121 Hawkins, F.J., Suzuki, S., Beermann, M.L., Barilla, C., Wang, R., Villacorta-Martin, C., Berical, A., Jean,
1122 J.C., Le Suer, J., Matte, T.*, et al.* (2021). Derivation of Airway Basal Stem Cells from Human Pluripotent
1123 Stem Cells. Cell Stem Cell *28*, 79-95 e78.
1124 Hayashi, K., Ohta, H., Kurimoto, K., Aramaki, S., and Saitou, M. (2011). Reconstitution of the mouse
1125 germ cell specification pathway in culture by pluripotent stem cells. Cell *146*, 519-532.
1126 Heinz, S., Benner, C., Spann, N., Bertolino, E., Lin, Y.C., Laslo, P., Cheng, J.X., Murre, C., Singh, H., and
1127 Glass, C.K. (2010). Simple combinations of lineage-determining transcription factors prime cis-
1128 regulatory elements required for macrophage and B cell identities. Mol Cell *38*, 576-589.
1129 Hever, A.M., Williamson, K.A., and van Heyningen, V. (2006). Developmental malformations of the eye:
1130 the role of PAX6, SOX2 and OTX2. Clin Genet *69*, 459-470.
1131 Jaeger, M.G., and Winter, G.E. (2021). Fast-acting chemical tools to delineate causality in transcriptional
1132 control. Mol Cell *81*, 1617-1630.
1133 Jiang, W., Zhang, D., Bursac, N., and Zhang, Y. (2013). WNT3 is a biomarker capable of predicting the
1134 definitive endoderm differentiation potential of hESCs. Stem Cell Reports *1*, 46-52.
1135 Jin, O., Harpal, K., Ang, S.L., and Rossant, J. (2001). Otx2 and HNF3beta genetically interact in anterior
1136 patterning. Int J Dev Biol *45*, 357-365.
1137 Kanai-Azuma, M., Kanai, Y., Gad, J.M., Tajima, Y., Taya, C., Kurohmaru, M., Sanai, Y., Yonekawa, H.,
1138 Yazaki, K., Tam, P.P.*, et al.* (2002). Depletion of definitive gut endoderm in Sox17-null mutant mice.
1139 Development *129*, 2367-2379.
1140 Kimura, C., Yoshinaga, K., Tian, E., Suzuki, M., Aizawa, S., and Matsuo, I. (2000). Visceral endoderm
1141 mediates forebrain development by suppressing posteriorizing signals. Dev Biol *225*, 304-321.

36

1142 Kimura-Yoshida, C., Nakano, H., Okamura, D., Nakao, K., Yonemura, S., Belo, J.A., Aizawa, S., Matsui, Y.,
1143 and Matsuo, I. (2005). Canonical Wnt signaling and its antagonist regulate anterior-posterior axis
1144 polarization by guiding cell migration in mouse visceral endoderm. Dev Cell *9*, 639-650.
1145 Kinoshita, M., Barber, M., Mansfield, W., Cui, Y., Spindlow, D., Stirparo, G.G., Dietmann, S., Nichols, J.,
1146 and Smith, A. (2020). Capture of Mouse and Human Stem Cells with Features of Formative
1147 Pluripotency. Cell Stem Cell.
1148 Kojima, Y., Yamashiro, C., Murase, Y., Yabuta, Y., Okamoto, I., Iwatani, C., Tsuchiya, H., Nakaya, M.,
1149 Tsukiyama, T., Nakamura, T.*, et al.* (2021). GATA transcription factors, SOX17 and TFAP2C, drive the
1150 human germ-cell specification program. Life Sci Alliance *4*.
1151 Langmead, B., and Salzberg, S.L. (2012). Fast gapped-read alignment with Bowtie 2. Nat Methods *9*,
1152 357-359.
1153 Li, H., Handsaker, B., Wysoker, A., Fennell, T., Ruan, J., Homer, N., Marth, G., Abecasis, G., Durbin, R.,
1154 and Genome Project Data Processing, S. (2009). The Sequence Alignment/Map format and SAMtools.
1155 Bioinformatics *25*, 2078-2079.
1156 Liao, Y., Smyth, G.K., and Shi, W. (2014). featureCounts: an efficient general purpose program for
1157 assigning sequence reads to genomic features. Bioinformatics *30*, 923-930.
1158 Liu, J., Yang, M., Zhao, W., and Zhou, X. (2022). CCPE: cell cycle pseudotime estimation for single cell
1159 RNA-seq data. Nucleic Acids Res *50*, 704-716.
1160 Loh, K.M., Ang, L.T., Zhang, J., Kumar, V., Ang, J., Auyeong, J.Q., Lee, K.L., Choo, S.H., Lim, C.Y., Nichane,
1161 M.*, et al.* (2014). Efficient endoderm induction from human pluripotent stem cells by logically directing
1162 signals controlling lineage bifurcations. Cell Stem Cell *14*, 237-252.
1163 Matsuo, I., Kuratani, S., Kimura, C., Takeda, N., and Aizawa, S. (1995). Mouse Otx2 functions in the
1164 formation and patterning of rostral head. Genes Dev *9*, 2646-2658.
1165 Medina-Cano, D., Corrigan, E.K., Glenn, R.A., Islam, M.T., Lin, Y., Kim, J., Cho, H., and Vierbuchen, T.
1166 (2022). Rapid and robust directed differentiation of mouse epiblast stem cells into definitive endoderm
1167 and forebrain organoids. Development *149*.
1168 Molder, F., Jablonski, K.P., Letcher, B., Hall, M.B., Tomkins-Tinch, C.H., Sochat, V., Forster, J., Lee, S.,
1169 Twardziok, S.O., Kanitz, A.*, et al.* (2021). Sustainable data analysis with Snakemake. F1000Res *10*, 33.
1170 Moore, R., Tao, W., Smith, E.R., and Xu, X.X. (2014). The primitive endoderm segregates from the
1171 epiblast in beta1 integrin-deficient early mouse embryos. Mol Cell Biol *34*, 560-572.
1172 Morgani, S.M., and Hadjantonakis, A.K. (2020). Signaling regulation during gastrulation: Insights from
1173 mouse embryos and in vitro systems. Curr Top Dev Biol *137*, 391-431.
1174 Morgani, S.M., and Hadjantonakis, A.K. (2021). Spatially Organized Differentiation of Mouse Pluripotent
1175 Stem Cells on Micropatterned Surfaces. Methods Mol Biol *2214*, 41-58.
1176 Morgani, S.M., Metzger, J.J., Nichols, J., Siggia, E.D., and Hadjantonakis, A.K. (2018). Micropattern
1177 differentiation of mouse pluripotent stem cells recapitulates embryo regionalized cell fate patterning.
1178 Elife *7*.
1179 Muncie, J.M., Ayad, N.M.E., Lakins, J.N., Xue, X., Fu, J., and Weaver, V.M. (2020). Mechanical Tension
1180 Promotes Formation of Gastrulation-like Nodes and Patterns Mesoderm Specification in Human
1181 Embryonic Stem Cells. Dev Cell *55*, 679-694 e611.
1182 Murphy, D., Salataj, E., Di Giammartino, D.C., Rodriguez-Hernaez, J., Kloetgen, A., Garg, V., Char, E.,
1183 Uyehara, C.M., Ee, L.S., Lee, U.*, et al.* (2023). Systematic mapping and modeling of 3D enhancer-
1184 promoter interactions in early mouse embryonic lineages reveal regulatory principles that determine
1185 the levels and cell-type specificity of gene expression. bioRxiv.

1186 Nabet, B., Ferguson, F.M., Seong, B.K.A., Kuljanin, M., Leggett, A.L., Mohardt, M.L., Robichaud, A.,
1187 Conway, A.S., Buckley, D.L., Mancias, J.D*., et al.* (2020). Rapid and direct control of target protein levels
1188 with VHL-recruiting dTAG molecules. Nat Commun *11*, 4687.
1189 Nabet, B., Roberts, J.M., Buckley, D.L., Paulk, J., Dastjerdi, S., Yang, A., Leggett, A.L., Erb, M.A., Lawlor,
1190 M.A., Souza, A*., et al.* (2018). The dTAG system for immediate and target-specific protein degradation.
1191 Nat Chem Biol *14*, 431-441.
1192 Navarra, A., Musto, A., Gargiulo, A., Petrosino, G., Pierantoni, G.M., Fusco, A., Russo, T., and Parisi, S.
1193 (2016). Hmga2 is necessary for Otx2-dependent exit of embryonic stem cells from the pluripotent
1194 ground state. BMC Biol *14*, 24.
1195 Nowotschin, S., Setty, M., Kuo, Y.Y., Liu, V., Garg, V., Sharma, R., Simon, C.S., Saiz, N., Gardner, R., Boutet,
1196 S.C*., et al.* (2019). The emergent landscape of the mouse gut endoderm at single-cell resolution. Nature
1197 *569*, 361-367.
1198 Pan, F.C., Evans, T., and Chen, S. (2020). Modeling endodermal organ development and diseases using
1199 human pluripotent stem cell-derived organoids. J Mol Cell Biol *12*, 580-592.
1200 Pannese, M., Polo, C., Andreazzoli, M., Vignali, R., Kablar, B., Barsacchi, G., and Boncinelli, E. (1995). The
1201 Xenopus homologue of Otx2 is a maternal homeobox gene that demarcates and specifies anterior body
1202 regions. Development *121*, 707-720.
1203 Pijuan-Sala, B., Griffiths, J.A., Guibentif, C., Hiscock, T.W., Jawaid, W., Calero-Nieto, F.J., Mulas, C., Ibarra-
1204 Soria, X., Tyser, R.C.V., Ho, D.L.L*., et al.* (2019). A single-cell molecular map of mouse gastrulation and
1205 early organogenesis. Nature *566*, 490-495.
1206 Prozzillo, Y., Fattorini, G., Santopietro, M.V., Suglia, L., Ruggiero, A., Ferreri, D., and Messina, G. (2020).
1207 Targeted Protein Degradation Tools: Overview and Future Perspectives. Biology (Basel) *9*.
1208 Qiu, C., Cao, J., Martin, B.K., Li, T., Welsh, I.C., Srivatsan, S., Huang, X., Calderon, D., Noble, W.S.,
1209 Disteche, C.M*., et al.* (2022). Systematic reconstruction of cellular trajectories across mouse
1210 embryogenesis. Nat Genet *54*, 328-341.
1211 Quinlan, A.R., and Hall, I.M. (2010). BEDTools: a flexible suite of utilities for comparing genomic
1212 features. Bioinformatics *26*, 841-842.
1213 Rhinn, M., Dierich, A., Le Meur, M., and Ang, S. (1999). Cell autonomous and non-cell autonomous
1214 functions of Otx2 in patterning the rostral brain. Development *126*, 4295-4304.
1215 Rhinn, M., Dierich, A., Shawlot, W., Behringer, R.R., Le Meur, M., and Ang, S.L. (1998). Sequential roles
1216 for Otx2 in visceral endoderm and neuroectoderm for forebrain and midbrain induction and
1217 specification. Development *125*, 845-856.
1218 Schindelin, J., Arganda-Carreras, I., Frise, E., Kaynig, V., Longair, M., Pietzsch, T., Preibisch, S., Rueden, C.,
1219 Saalfeld, S., Schmid, B*., et al.* (2012). Fiji: an open-source platform for biological-image analysis. Nat
1220 Methods *9*, 676-682.
1221 Seah, M.K.Y., Wang, Y., Goy, P.A., Loh, H.M., Peh, W.J., Low, D.H.P., Han, B.Y., Wong, E., Leong, E.L., Wolf,
1222 G*., et al.* (2019). The KRAB-zinc-finger protein ZFP708 mediates epigenetic repression at RMER19B
1223 retrotransposons. Development *146*.
1224 Setty, M., Kiseliovas, V., Levine, J., Gayoso, A., Mazutis, L., and Pe'er, D. (2019). Characterization of cell
1225 fate probabilities in single-cell data with Palantir. Nat Biotechnol *37*, 451-460.
1226 Simeone, A. (1998). Otx1 and Otx2 in the development and evolution of the mammalian brain. EMBO J
1227 *17*, 6790-6798.
1228 Skene, P.J., Henikoff, J.G., and Henikoff, S. (2018). Targeted in situ genome-wide profiling with high
1229 efficiency for low cell numbers. Nat Protoc *13*, 1006-1019.
1230 Skene, P.J., and Henikoff, S. (2017). An efficient targeted nuclease strategy for high-resolution mapping
1231 of DNA binding sites. Elife *6*.

Spieler, D., Baumer, N., Stebler, J., Koprunner, M., Reichman-Fried, M., Teichmann, U., Raz, E., Kessel, M., and Wittler, L. (2004). Involvement of Pax6 and Otx2 in the forebrain-specific regulation of the vertebrate homeobox gene ANF/Hesx1. Dev Biol *269*, 567-579.

Takenaga, M., Fukumoto, M., and Hori, Y. (2007). Regulated Nodal signaling promotes differentiation of the definitive endoderm and mesoderm from ES cells. J Cell Sci *120*, 2078-2090.

Tam, P.P., and Behringer, R.R. (1997). Mouse gastrulation: the formation of a mammalian body plan. Mech Dev *68*, 3-25.

Tam, P.P., and Loebel, D.A. (2007). Gene function in mouse embryogenesis: get set for gastrulation. Nat Rev Genet *8*, 368-381.

Tang, W.W.C., Castillo-Venzor, A., Gruhn, W.H., Kobayashi, T., Penfold, C.A., Morgan, M.D., Sun, D., Irie, N., and Surani, M.A. (2022). Sequential enhancer state remodelling defines human germline competence and specification. Nat Cell Biol *24*, 448-460.

Tesar, P.J., Chenoweth, J.G., Brook, F.A., Davies, T.J., Evans, E.P., Mack, D.L., Gardner, R.L., and McKay, R.D. (2007). New cell lines from mouse epiblast share defining features with human embryonic stem cells. Nature *448*, 196-199.

Tyser, R.C.V., Mahammadov, E., Nakanoh, S., Vallier, L., Scialdone, A., and Srinivas, S. (2021). Single-cell transcriptomic characterization of a gastrulating human embryo. Nature *600*, 285-289.

Uyehara, C.M., and Apostolou, E. (2023). 3D enhancer-promoter interactions and multi-connected hubs: Organizational principles and functional roles. Cell Rep, 112068.

Uyehara, C.M., Leatham-Jensen, M., and McKay, D.J. (2022). Opportunistic binding of EcR to open chromatin drives tissue-specific developmental responses. Proc Natl Acad Sci U S A *119*, e2208935119.

Wang, P., McKnight, K.D., Wong, D.J., Rodriguez, R.T., Sugiyama, T., Gu, X., Ghodasara, A., Qu, K., Chang, H.Y., and Kim, S.K. (2012). A molecular signature for purified definitive endoderm guides differentiation and isolation of endoderm from mouse and human embryonic stem cells. Stem Cells Dev *21*, 2273-2287.

White, M.A., Kwasnieski, J.C., Myers, C.A., Shen, S.Q., Corbo, J.C., and Cohen, B.A. (2016). A Simple Grammar Defines Activating and Repressing cis-Regulatory Elements in Photoreceptors. Cell Rep *17*, 1247-1254.

Wolf, F.A., Angerer, P., and Theis, F.J. (2018). SCANPY: large-scale single-cell gene expression data analysis. Genome Biol *19*, 15.

Yang, S.H., Kalkan, T., Morissroe, C., Marks, H., Stunnenberg, H., Smith, A., and Sharrocks, A.D. (2014). Otx2 and Oct4 drive early enhancer activation during embryonic stem cell transition from naive pluripotency. Cell Rep *7*, 1968-1981.

Yasuoka, Y., Suzuki, Y., Takahashi, S., Someya, H., Sudou, N., Haramoto, Y., Cho, K.W., Asashima, M., Sugano, S., and Taira, M. (2014). Occupancy of tissue-specific cis-regulatory modules by Otx2 and TLE/Groucho for embryonic head specification. Nat Commun *5*, 4322.

Yu, G., Wang, L.G., and He, Q.Y. (2015). ChIPseeker: an R/Bioconductor package for ChIP peak annotation, comparison and visualization. Bioinformatics *31*, 2382-2383.

Yu, P., Pan, G., Yu, J., and Thomson, J.A. (2011). FGF2 sustains NANOG and switches the outcome of BMP4-induced human embryonic stem cell differentiation. Cell Stem Cell *8*, 326-334.
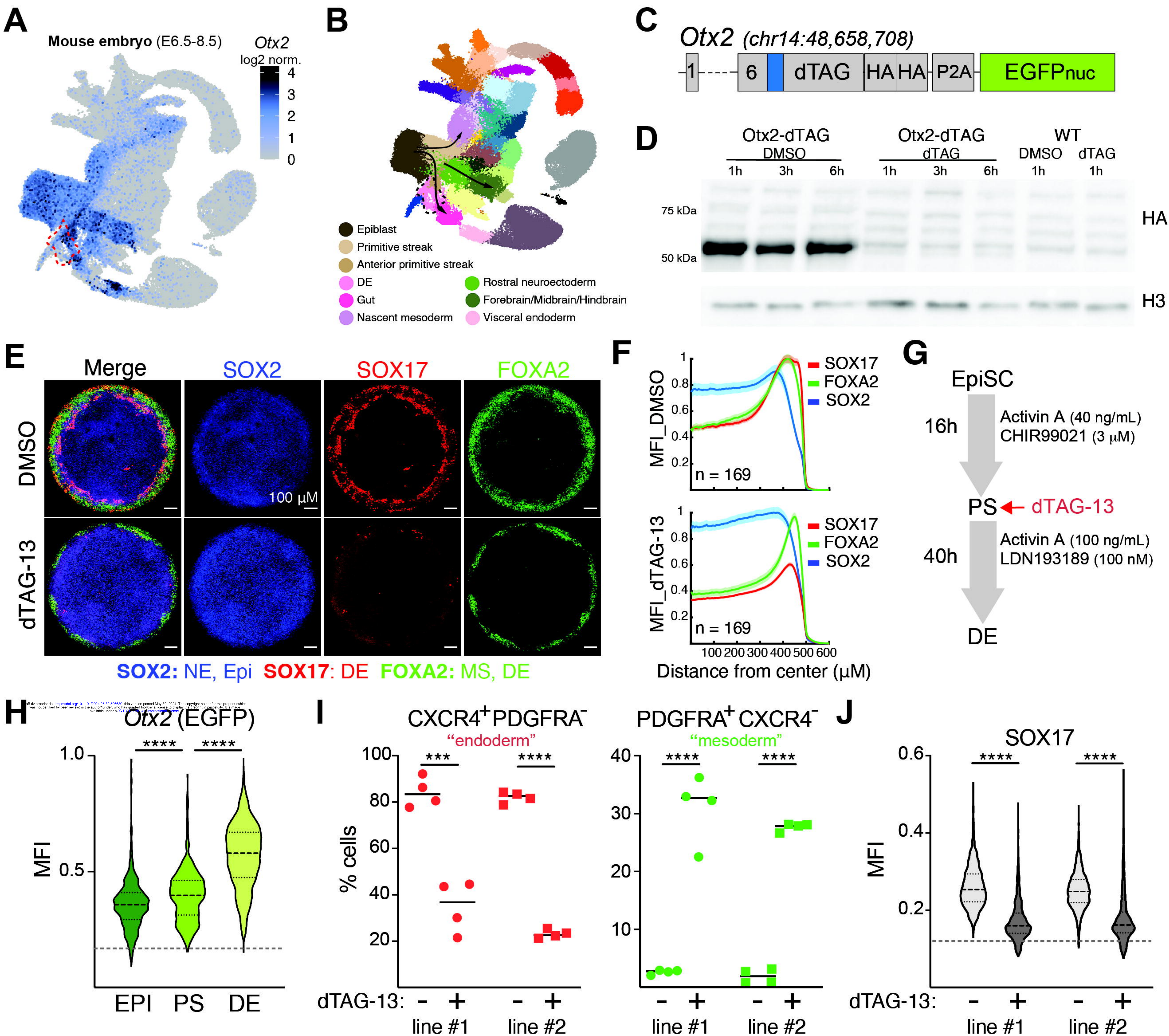
Zeng, B., Liu, Z., Lu, Y., Zhong, S., Qin, S., Huang, L., Zeng, Y., Li, Z., Dong, H., Shi, Y., *et al.* (2023). The single-cell and spatial transcriptional landscape of human gastrulation and early brain development. Cell Stem Cell *30*, 851-866 e857.

Zhang, J., Zhang, M., Acampora, D., Vojtek, M., Yuan, D., Simeone, A., and Chambers, I. (2018). OTX2 restricts entry to the mouse germline. Nature *562*, 595-599.

1277   Zhang, Y., Liu, T., Meyer, C.A., Eeckhoute, J., Johnson, D.S., Bernstein, B.E., Nusbaum, C., Myers, R.M.,
1278   Brown, M., Li, W.*, et al.* (2008). Model-based analysis of ChIP-Seq (MACS). Genome Biol *9*, R137.
1279   Zhong, L., Gordillo, M., Wang, X., Qin, Y., Huang, Y., Soshnev, A., Kumar, R., Nanjangud, G., James, D.,
1280   David Allis, C.*, et al.* (2023). Dual role of lipids for genome stability and pluripotency facilitates full
1281   potency of mouse embryonic stem cells. Protein Cell *14*, 591-602.
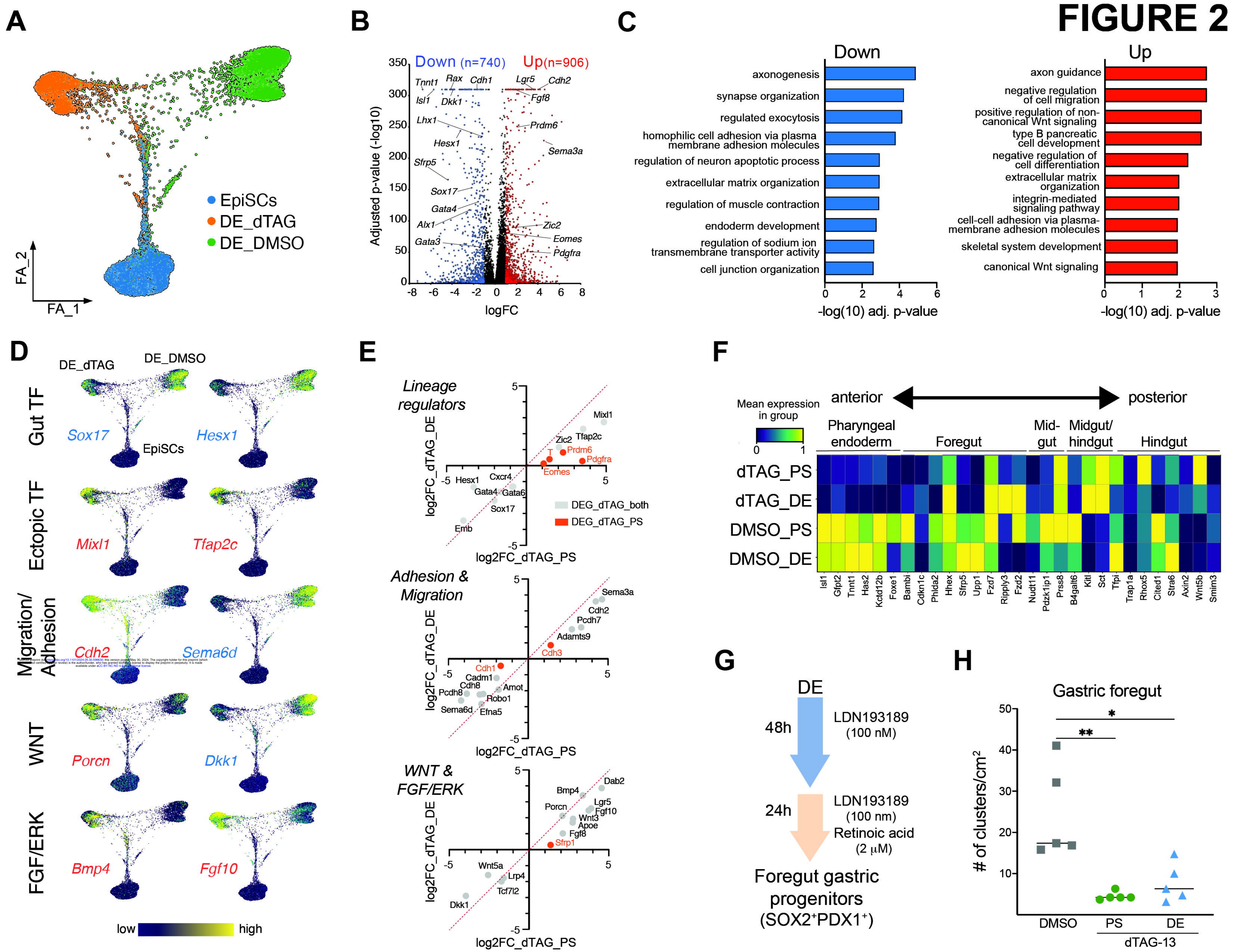1282

FIGURE 1

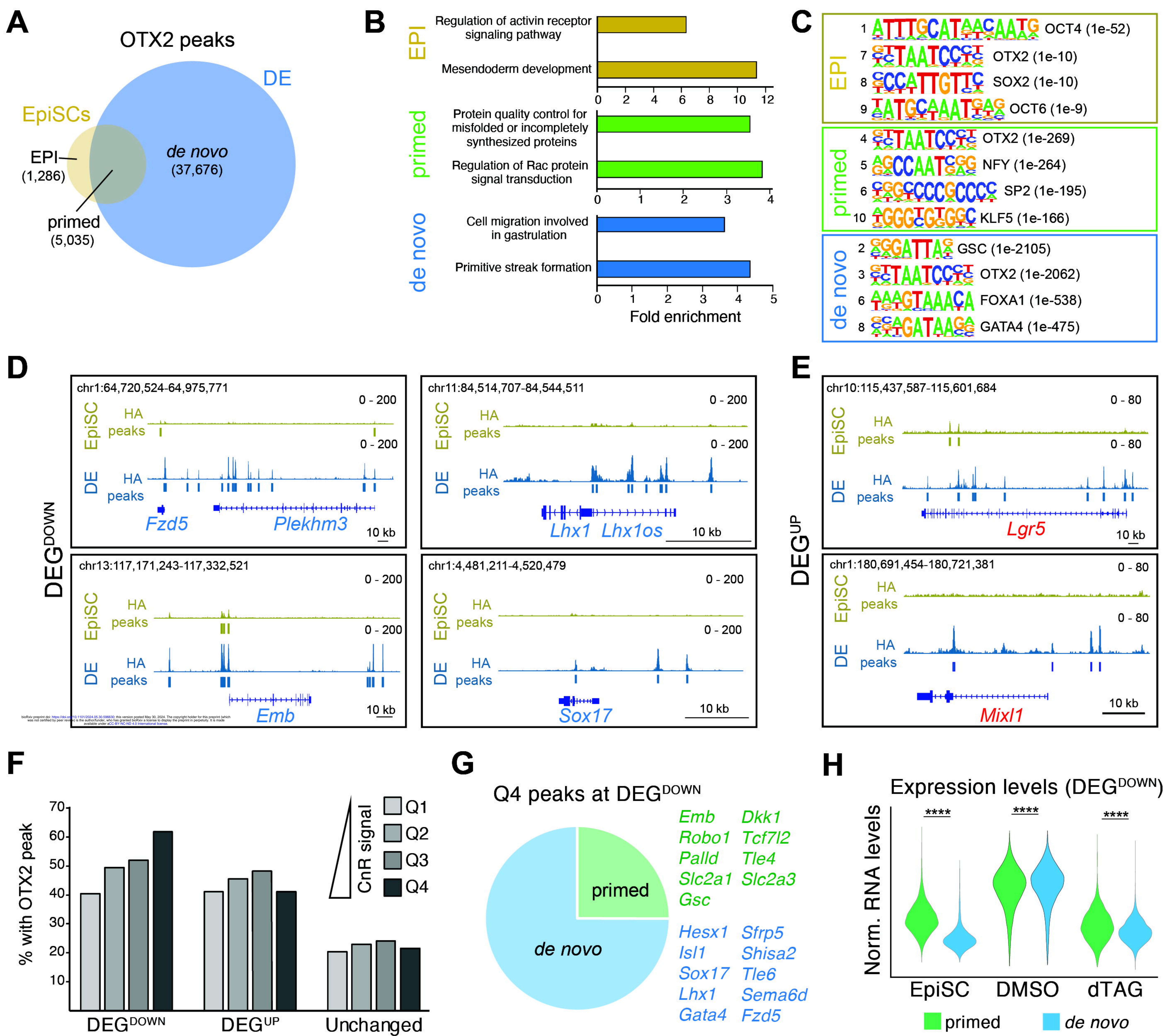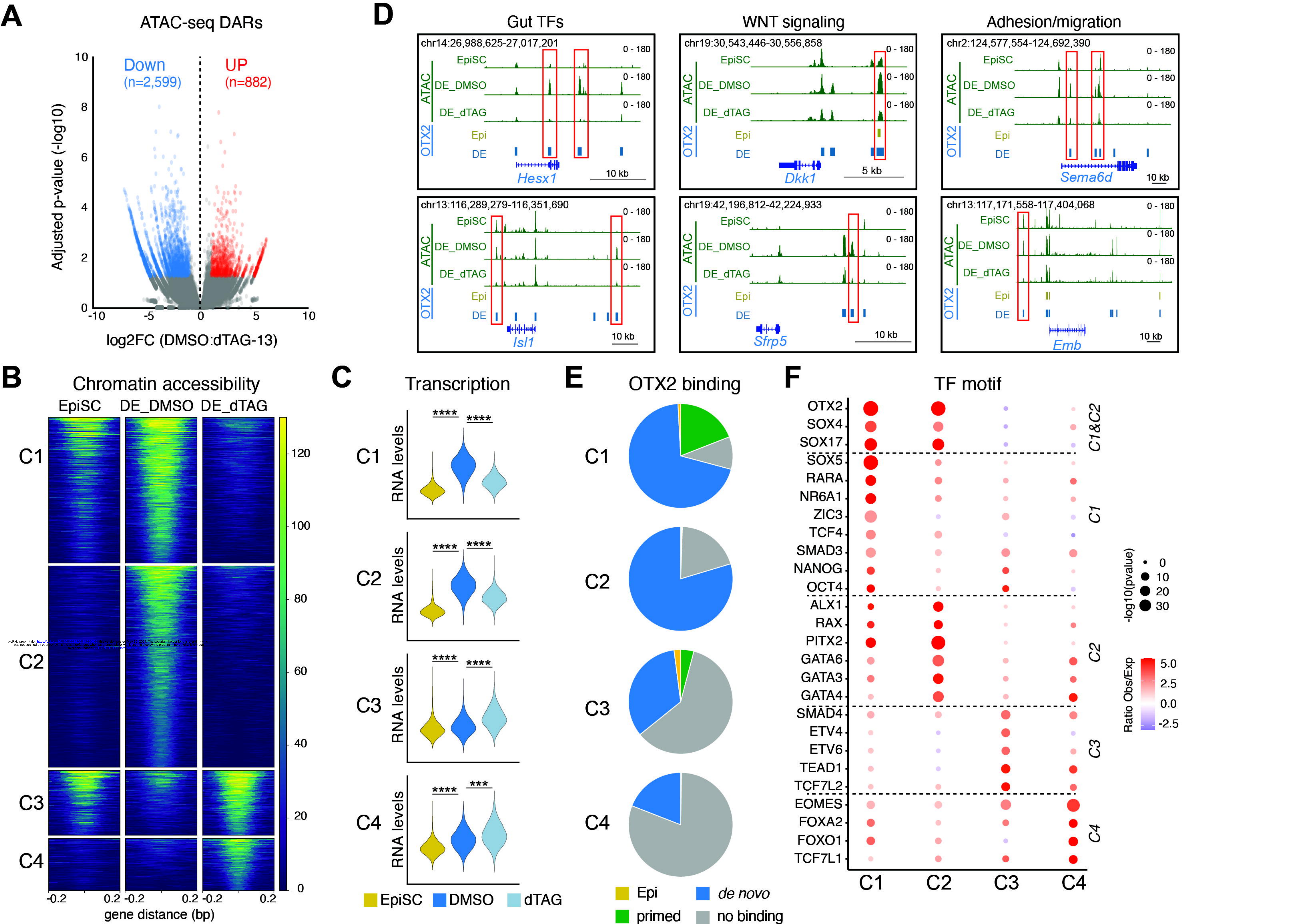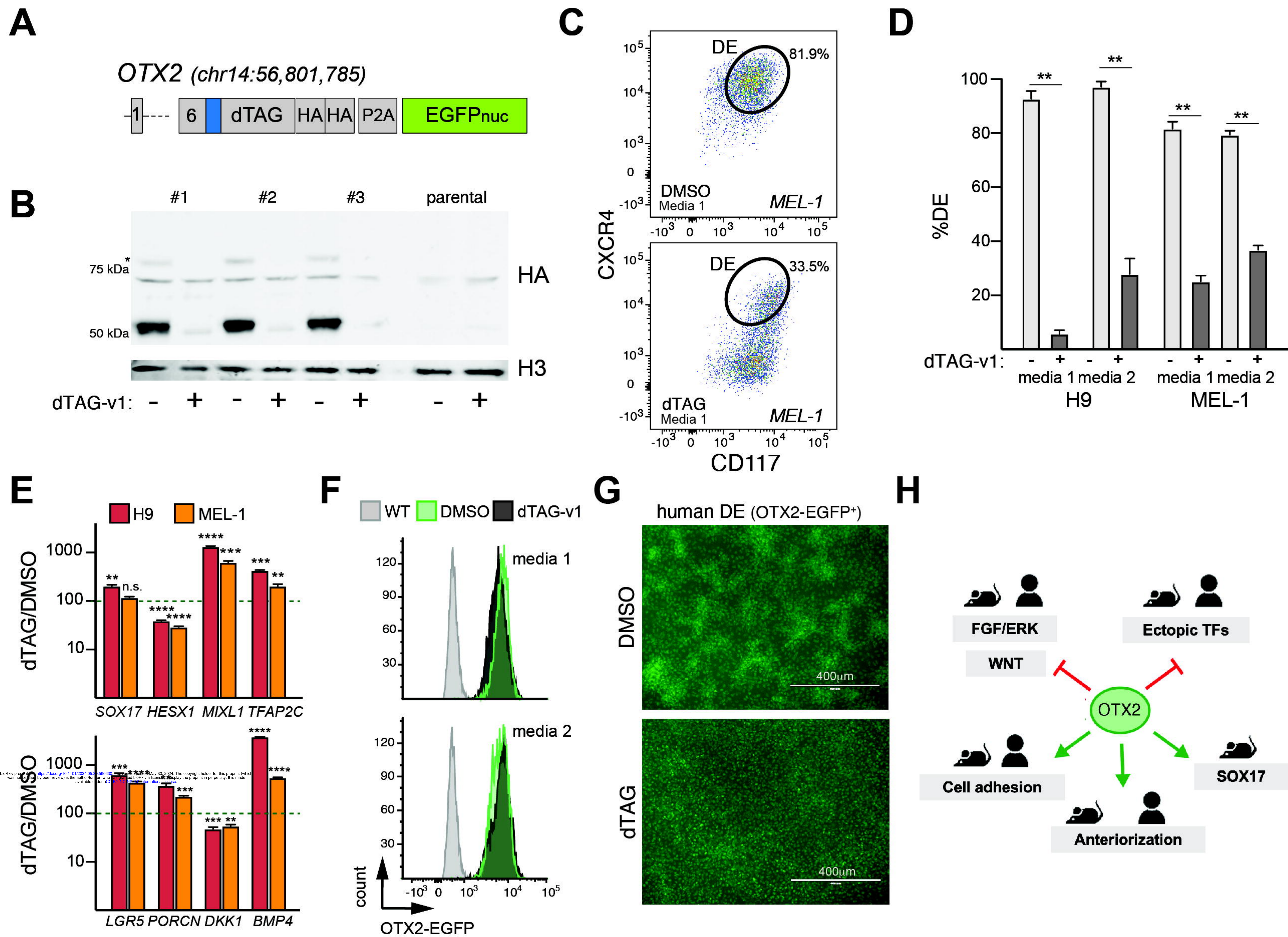A. Mouse embryo (E6.5-8.5) — *Otx2* log2 norm.

B. Cell type legend: Epiblast, Primitive streak, Anterior primitive streak, DE, Gut, Nascent mesoderm, Rostral neuroectoderm, Forebrain/Midbrain/Hindbrain, Visceral endoderm

C. *Otx2 (chr14:48,658,708)* — 1 ... 6 dTAG HA HA P2A EGFPnuc

D. Otx2-dTAG DMSO / Otx2-dTAG dTAG / WT DMSO dTAG — 1h 3h 6h; HA, H3; 75 kDa, 50 kDa

E. Merge, SOX2, SOX17, FOXA2; DMSO, dTAG-13; 100 µM
SOX2: NE, Epi SOX17: DE FOXA2: MS, DE

F. MFI_DMSO, MFI_dTAG-13 — SOX17, FOXA2, SOX2; n = 169; Distance from center (µM)

G. EpiSC → 16h Activin A (40 ng/mL) CHIR99021 (3 µM) → PS ← dTAG-13 → 40h Activin A (100 ng/mL) LDN193189 (100 nM) → DE

H. *Otx2* (EGFP) — MFI; EPI, PS, DE; ****

I. CXCR4+PDGFRA− "endoderm"; PDGFRA+CXCR4− "mesoderm"; % cells; dTAG-13: − + line #1, − + line #2; ***, ****

J. SOX17 — MFI; dTAG-13: − + line #1, − + line #2; ****

FIGURE 2

FIGURE 3

FIGURE 4

A ATAC-seq DARs

B Chromatin accessibility

C Transcription

D Gut TFs · WNT signaling · Adhesion/migration

E OTX2 binding

F TF motif

FIGURE 5

A

EpiLC:ESC
FC>5; padj<0.05

In vivo kinetics?

All mouse TFs (n=1,682) → Epiblast TFs (n=29) →

Otx2 (49.7x)
Zic3 (15.4x)
Zic5 (11.9x)
Pou3f1 (13.0x)
Zic2 (11.4x)
Sall1 (6.2x)
Rarg (5.8x)

B Otx2 — log2 nomr. counts

Epiblast, Primitive Streak, DE, Visceral endoderm, Rostral NE, ExE endoderm, PGC

C % OTX2-EGFP+ — ESC, EpiLC, EpiSC

D

plating   WNT3a

Fibronectin | Laminin
FGF2/ACTIVIN A (F/A)

-72h -48h -24h 0h 24h 48h

ESCs   EpiLCs   dTAG-13   Gastruloid analysis

bioRxiv preprint doi: https://doi.org/10.1101/2024.05.30.596630; this version posted May 30, 2024. The copyright holder for this preprint (which was not certified by peer review) is the author/funder, who has granted bioRxiv a license to display the preprint in perpetuity. It is made available under aCC-BY-NC-ND 4.0 International license.

E OCT4 / T / SOX17 — MFI — EPI PS DE

F HA — MFI — dTAG-13: KI(-) KI(+) WT(+)

G parental (WT) / OTX2-dTAG — DMSO / dTAG-13
CXCR4 ("endoderm") vs PDGFRA ("mesoderm")

H SOX17 — MFI — dTAG-13: (-) (+) parental (WT)

I CXCR4 — MFI (dTAG-13/DMSO)
KI/WT ratio: KI only, 4:1, 1:4, WT only, 4:1, 1:4
OTX2-dTAG (KI) cells / parental (WT) cells

A

CUT&RUN signal

EpiSC KI DE KI DE WT

EPI only

DE only

common

gene distance (bp)

B

Signal intesity (reads)

in EpiSCs
in DE

****

****

****

EPI   primed   de novo

OTX2 peaks

C

EPI

primed

de novo

distal intergenic
promoter
intron
3' UTR
exon
downstream

D

chr17:35,499,878-35,511,290

EpiSC HA peaks

DE HA peaks

0 - 200

0 - 200

5 kb

Pou5f1

E

DEG^DOWN
DEG^UP
unchanged

% of genes

with non-promoter peak   with promoter peak   with any peak

F

OTX2 peaks per gene

ns
****
****

DOWN   UP   unchanged

G

promoter   non-promoter

Signal intesity (reads)

**
****
*

****
****
ns

DOWN UP unchanged   DOWN UP unchanged

H

primed   *de novo*

DEG^DOWN

2   106   239

DEG^UP

5   107   276

A Percentage of ATAC-seq peaks

ATAC DE>EpiSC (n=45,727)
ATAC EpiSC>DE (n=41,677)

not OTX2 bound
OTX2 bound in DE
OTX2 bound in EpiSC
OTX2 bound in EpiSC & DE

B ATAC-seq

$\log_2 FC$ (dTAG:DMSO) vs BaseMean

DAR^{UP} (n=882)
DAR^{DOWN} (n=2,599)

C DARs (DMSO vs dTAG)

non-DAR (EpiSC vs DE)
DAR (EpiSC vs DE)

D Distribution

C1, C2, C3, C4, control sites

Promoter, Distal, Intron, Other

E DARs at DEGs

DEG^{DOWN}, DEG^{UP}, control

C1, C2, C3, C4, no DAR

F OTX2 binding strength

EpiSC — HA CnR signal — C1, C2, C3, C4, All peaks
**** ns ns ns

DE — HA CnR signal — C1, C2, C3, C4, All peaks
**** ns ns ns

G TF motifs

C1&C2: OTX2, SOX4, SOX17
C1: SOX5, RARA, NR6A1, ZIC3, TCF4, SMAD3, NANOG, OCT4
C2: ALX1, RAX, PITX2, GATA6, GATA3, GATA4
C3: SMAD4, ETV4, ETV6
C3&C4: TEAD1, TCF7L2, EOMES
C4: FOXA2, FOXO1, TCF7L1

OTX2 bound: Y N Y N Y N Y N
C1 C2 C3 C4

Row Z-Score −2 0 2

A

% conservation DE-associated TFs
(mouse vs human)

LHX1
OTX2
HHEX
FOXA2
GATA4
EOMES
GATA6
SOX17
FOXA3
HESX1

50 60 70 80 90 100

B

parental_DMSO   KI_DMSO
OTX2 (HA)
200μm   200μm

KI_dTAG13   KI_dTAGv1
OTX2 (HA)
200μm   200μm

C

Protocol 1 (Medina-Cano et al., 2022)

hESC → 24h → PS → 48h → DE

Activin A (40 ng/mL)   Activin A (100 ng/mL)
CHIR99021 (3 μM)   LDN193189 (100 nM)

Protocol 2 (Loh et al., 2014)

hESC → 24h → PS → 48h → DE

Activin A (100 ng/mL)   Activin A (100 ng/mL)
CHIR99021 (2 μM)   LDN193189 (250 nM)
PIK90 (100 μM)

D

%OTX2-EGFP+ cells

H9   MEL-1

hESC   DE (media1)   DE (media2)

E

MFI_OTX2

**** ****
****

*** ****

H9   MEL-1

hESC   DE (media1)   DE (media2)

F

SOX17   DAPI

dTAG-v1

DMSO